On the Fluid Mechanics of Viscoplastic Particle Suspension Fractionation: Understanding Multilayer Spiral Poiseuille Flow in an Annulus

by

Mohammad Al-Shibl

B.Sc., Mechanical Engineering, King Saud University, 1993
M.Sc., Mechanical Engineering, King Fahd University of Petroleum and Minerals, 2006

A THESIS SUBMITTED IN PARTIAL FULFILLMENT OF
THE REQUIREMENTS FOR THE DEGREE OF

DOCTOR OF PHILOSOPHY

in

The Faculty of Graduate and Postdoctoral Studies

(Chemical and Biological Engineering)

THE UNIVERSITY OF BRITISH COLUMBIA

(Vancouver)

July 2016

Abstract

The focus of the present work is the study of laminar spiral multi-layer viscoplastic flow in annular geometries. The motivation for the present work stems from an interest in utilizing such flow in fractionation of particle suspensions. The work is presented in four studies.

In the first study we solve the fully developed condition of the flow analytically. This solution is considered a reliable reference to validate the remaining numerical studies. Also it provides a means to test the stability of the flow.

The second study is related to the fractionation of particle suspensions utilizing the solution demonstrated in the first study. We develop fractionation curves of particles of different sizes in fluids with different rheology. We develop a code to simulate thousands of flow cases (a flow case has a unique combination of streams flowrates) of known fluids properties. We predict the fractionation operating window (some range of streams flowrates) needed for successful fractionation.

Abstract

In the third study, we examine the flow in the full annulus geometry including the entrance region of the flow. Here, we estimate the flow entrance length in order to design the length of the mixing zone of the two streams in the continuous fractionation device. We study the effect of Kelvin-Helmholtz and density current instabilities on the flow.

In the fourth study, we attempt to design the continuous fractionation device in which we use the results of the first three studies together with the analysis of the constraints imposed by the physical construction of the device. We explore the flow behavior in the exit region of the device and suggest some guidelines to achieve successful fractionation accordingly.

Results of this work show that spiral multi-layer Poisuille viscoplastic flow can be stable and the range of stability expands with increasing fluids yield stress. Gravity current instability is evident in density unstable cases and the flow can be stabilized by increasing the fluids yield stress. Kelvin Helmholtz instability was not found on conditions tested. Viscoplastic flow entrance length was found to be shorter than the equivalent Newtonian one for the same range of Reynolds number.

Preface

Three chapters of this thesis will be submitted for publication in refereed journals. Following are the detail of the submission:

1. Chapter three, Alshibl M. and Martinez D.M. Continuous fractionation of particle suspensions in a viscoplastic fluid using spiral multi-layer Poiseuille flow. I solved the flow analytically, conducted the study and wrote the paper under the supervision of Dr. Martinez.

2. Chapter four, Alshibl M. and Martinez D.M. Study of entrance region spiral multi-layer Poiseuille flow of viscoplastic fluid in annular geometries with density current effects. Dr. Martinez supervised the research and I solved the flow numerically, validated the solution, planned and performed the simulations.

3. Chapter five, Alshibl M. and Martinez D.M. Study of the operation and efficiency of the continuous fractionation system of particle suspensions in a viscoplastic fluid using spiral multi-layer Poiseuille flow.

This research has been supervised by Dr. Martinez. I designed the device, solved the flow numerically, validated the solution, planned and performed the simulations.

Table of Contents

Appendices

List of Tables

List of Figures

Nomenclature

Roman letters

$\hat{G}$ Pressure drop rate Pa/m

$\hat{p}$ Pressure Pa

$\hat{Q}$ Flow rate kg/m^3

$\hat{R}$ Annulus outer radius m

$\hat{r}$ Radial position m

$\hat{R}_i$ Annulus inner radius m

$\hat{u}$ Velocity m/s

$\hat{U}_o$ Characteristic velocity m/s

At Atwood number

B Bingham number

Nomenclature

D_h	Hydraulic diameter	m
F	Applied force	N
L_e	Entrance length	m
Re	Reynolds number	
Ri	Richardson number	

Subscripts

θ	Tangential	
c	Critical	
r	Radial	
z	Axial	

Greek letters

τ	Shear stress	Pa
τ_y	Yield stress	Pa
α	Concentration	
γ	Shear rate	s^{-1}
$\hat{\omega}$	Rotational speed	rad/s

κ	Annulus radius ratio	
μ	Dynamic viscosity	$pa.s$
ρ	Density	kg/m^3

Acknowledgements

Acknowledgment is due to the College of Engineering of King Saud University for supporting this research.

I would like to express my sincere gratitude to my advisor Prof. Mark Martinez for the continuous support of my Ph.D study and related research, for his patience, motivation, and immense knowledge. His guidance helped me in all the time of research and writing of this thesis. I could not have imagined having a better advisor for my Ph.D study.

Besides my advisor, I would like to thank the rest of my thesis committee: Dr. Kendal Bushe, and Dr. Heather Trajano, for their insightful comments and encouragement, but also for the hard question which incented me to widen my research from various perspectives.

Last but not the least, I would like to thank my parents and my family for supporting me spiritually throughout writing this thesis and my life in general.

Dedication

<div dir="rtl">

بِسْمِ اللهِ الرَّحْمنِ الرَّحِيمِ

(هَذَا مِن فَضْلِ رَبِّي لِيَبْلُوَنِي أَأَشْكُرُ أَمْ أَكْفُرُ وَمَن شَكَرَ فَإِنَّمَا يَشْكُرُ
لِنَفْسِهِ وَمَن كَفَرَ فَإِنَّ رَبِّي غَنِيٌّ كَرِيمٌ)

سورة النمل – اية ٤٠

</div>

"This is from the favor of my Lord to test me whether I will be grateful or ungrateful. And whoever is grateful - his gratitude is only for [the benefit of] himself. And whoever is ungrateful - then indeed, my Lord is Free of need and Generous." [The holy Quran, Surah An-Naml, verse 40.]

<div dir="rtl">

«اللهم ربَّنا لك الحمدُ مِلءَ السماءَ، ومِلءَ الأرضِ،ومِلءَ ما بينَهما، ومِلءَ ما
شِئتَ من شيءٍ بعدُ»

رواه مسلم

</div>

"All praise is due to you ,O Lord and The heavens and the Earth and all between them abound with Your praises, and all that You will abounds with Your praises the way that Allah loves and pleases Him...." [Narrated by Muslim]

Chapter 1

Introduction

The focus of the present work is the study of laminar multi-layer viscoplastic flow in annular geometries as shown in figure 1.1. This type of flow is used in the novel fractionation process of particle suspensions that was advanced by Madani et al. (2010b). They proved this new fractionation methodology on a batch wise basis. The purpose of this work is to extend the new method applicability to continuous fractionation for use in industrial applications.
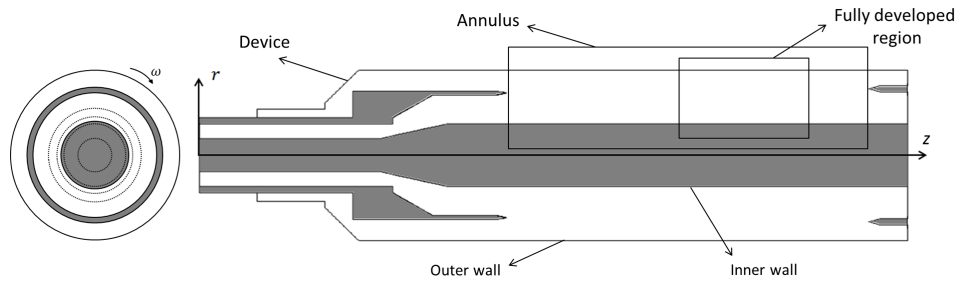
Figure 1.1: A schematic of the geometry showing the fully developed region, the annulus and the fractionation device.

The motivation for the present work stems from an interest in the frac-

tionation of particle suspensions especially with papermaking fibre suspensions. Fractionation is a vital part in papermaking process. It allows the processing of low quality fractions of pulp suspensions to improve paper quality and reduce the consumption of the required chemicals, energy or assets.

Additionally, it enables papermakers to produce products over a wide range of properties that can be used in different applications. To elaborate more, if we fractionate a mixture of long and short pulp fiber suspension, we are going to get a short fiber fraction that is known for having better printing capabilities and a long fiber fraction that has a higher tensile strength. In addition to that, we can blend these fractions at different ratios to get different paper products with a variety of properties that can be used in different paper applications.

We conducted four different but complementary studies to facilitate this multi-layer flow in the continuous fractionation process, these studies are carried out in order to design an industially applicable process. The first study deals with the fully developed condition of the flow. This condition allows us to solve the problem analytically and hence provide a reliable reference to validate the remaining numerical studies. This solution also provides a means to test the stability of the flow.

The second study is related to the fractionation of particles in particles suspensions utilizing the solution demonstrated in the first study. We develop particle fractionation curves of particles of different sizes in fluids with different rheology. We develop a code to simulate thousands of flow cases (a flow case has a unique combination of streams flowrates) that we may have for fluids of known rheology and for particles of different sizes. We predict the fractionation operating window (some range of streams flowrates) needed for successful fractionation.

In the third study, we examine the flow in a full annulus geometry including the entrance region of the flow. Here, we estimate the flow entrance length in order to design the length of the mixing zone of the two streams in the continuous fractionation device. We study the effect of Kelvin-Helmholtz and density current instabilities on the flow.

In the fourth study, we attempt to design the continuous fractionation device in which we use the results of the first three studies together with the analysis of the constraints imposed by the physical construction of the device. We explore the flow behavior in the exit region of the device and suggest some guidelines to achieve successful fractionation accordingly.

This thesis is presented in 6 chapters. In chapter 1 we present the motivation of this work. Chapter 2 gives a background on the fractionation

methods, fractionation efficiency, presents the new fractionation principle and the potential flow characteristics to be used in this new methodology. The fully developed flow problem and particle fractionation studies are presented in chapter 3. We present the full annulus problem solution and density current analysis in chapter 4 and the continuous fractionation device study in chapter 5. We end the work by conclusions in chapter 6 and bibliography.

Chapter 2

Background

In this chapter we will shed light on the available fractionation methods, their efficiency and the need for a new fractionation technique. We will discuss in more detail particle motion with both Newtonian and non-Newtonian suspensions as they are the core of the fractionation process. The proposed continuous fractionation device that employs the new technique is explored in terms of identifying the nature of the flow to be used.

2.1 The current pulp fractionation methods

Currently, there are two methods to fractionate pulp fibers: pressure screens (figure 2.1) and hydro-cyclones (figure 2.2). In pressure screens, the fiber suspension enters an annular gap between a rotor and an outer cylinder with small openings (either slots or holes), separation is then achieved based on the length of the fiber as small fibers pass through the openings. Pressure screens usually are equipped with different types of rotors that continuously

disperse fibers to prevent them from accumulating on the screen surface. A number of studies discuss pressure screens design and operation, for example, Sloane (2000) and Julien Saint Amand and Perrin (1999) gave a general review of pressure screening systems, their design and efficiency.
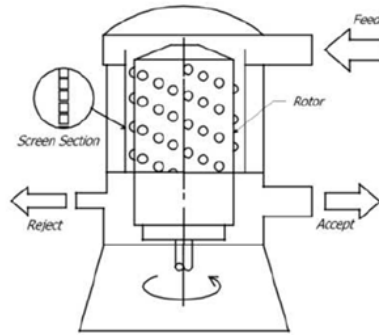
Figure 2.1: Schematic of a pressure screen.

On the other hand, hydrocyclones separate fibers based on their specific surface or surface area per gram, resulting in separation of large diameter thin walled fibers from small diameter thick walled ones. Hydrocyclones are conical or partly cylindrical devices with no moving parts. Here the pulp suspension flows into the hydrocyclone with a tangent angle creating a swirling flow. Due to centrifugal force the dense materials are pushed toward the outside and collected at the bottom of the hydrocyclone as rejects.

6
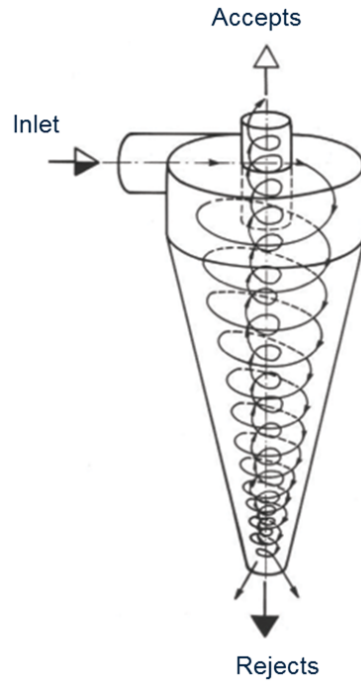
Figure 2.2:   Schematic of a hydrocyclone.

Paavilainen (1992) studied experimentally the hydrocyclone operation and showed that they are indeed able to fractionate fibers based on its specific surface.

Despite the fact that pressure screens and hydro-cyclones are considered the industrially approved methods, these methods have relatively low efficiencies. The flow within these devices is complex due to the stochastic nature of turbulence, the presence of boundaries, and the long range hydro-dynamic interactions between suspended fibers, Madani et al. (2010b). All

these facts have a negative impact on the efficiency of both pressure screens and hydro-cyclones.

To address the problem of low efficiency of these devices, we will explore fractionation efficiency in more detail. Fractionation efficiency is built upon an understanding of the motion of different classes of particles in a flowing Newtonian suspension. In the next section we briefly review a number of studies on particle motion for the purpose of understanding why the efficiency in these devices is low. Afterwards, we discuss particle behaviour in viscoplastic fluids and how this behaviour makes utilizing viscoplastic fluids in fractionation a wise decision.

The novel fractionation principle of Madani et al. (2010b) is then introduced with some preliminary results from batchwise experiments. Following that, the continuous fractionation method proposed by Madani et al. (2010b) using viscoplastic fluids is then introduced. And we finalize this chapter with an introduction to the academic problem.

2.2   Particles motion in Newtonian suspensions

The motion of particles in Newtonian suspensions is extremely complex. Studies by Batchelor (1972), and more recently by Mackaplow and Shaqfeh (1998) were concerned with the simplest case of settling of an isolated rod

in an unbounded fluid experiencing stokes flow described by the following equation.

$$\mathbf{V}_{sed} = \frac{\Delta\rho d^2}{16\mu}[(\ln 2r + 0.193 + O(\ln 2r)^{-1})\mathbf{g} + (\ln 2r - 1,807 + O(\ln 2r)^{-1})(\mathbf{p}\cdot\mathbf{g})\mathbf{p}]$$

(2.1)

where $\Delta\rho$ is the difference in density between the fibre density ρ and the surrounding fluid density ρ_f ; r is the aspect ratio of the fibre defined by l/d where d is the diameter of the fibre ; μ is the viscosity of the fluid ; $\mathbf{g}$ is the acceleration due to gravity ; and $\mathbf{p}$ is the unit vector that indicates fibre orientation.

They found that rods -based on their orientation- are subjected to lateral movement while settling vertically under the effect of gravity with the drift velocity strongly dependent on fiber orientation, this is not the case for spheres.

On the other hand Jayaweera and Mason (1965) reported that orientation does not affect settling at low Re, $(Re < 0.01)$ and cylinders fall with the same altitude that they were released with. We conclude that there is no unique terminal velocity for settling cylinders, and the terminal velocity depends on the orientation and aspect ratio of the cylinder. This difference in terminal velocities may give a basis for separating particles mechanically.

In more realistic situations, i.e., higher concentration and Reynolds numbers, long range disturbances are introduced to the system resulting in a distribution for the settling velocity. Disturbances are created by presence of other particles and/or increasing the Reynolds number.

Let us start looking at the effect of the 'wake of a moving particle in the vicinity of another. In this regard, Happel and Brenner (1965) explained that the physics becomes more complex as each individual fibre settles and rotates under the influence of the 'wakes' or 'long-range hydrodynamic disturbances' of the other settling particles. This in turn leads to inhomogeneous settling rates and local floc formation. Floc formation was observed also by Kumar and Ramarao (1991) in monodisperse glass fibre suspensions.

In an interesting finding, Herzhaft and Guazzelli (1999) reported that in the dilute regime, the ensemble-averaged settling velocity actually increases with concentration and may exceed the velocity of an isolated particle. They found also that most of the fibers are aligned in the direction of gravity under these flow conditions.

Some numerical simulations conducted by (Mackaplow and Shaqfeh (1998); Butler and Shaqfeh (2002); Koch and Shaqfeh (1989)) for the flow under these conditions and in the limit of $Re = 0$, using slender body theory, suggested that the settling suspension should segregate into particle

clumps. The simulations were in good agreement with experimental results of Herzhaft and Guazzelli (1999).

For higher Reynolds numbers which are more relevant to the paper-making industry, Marton and Robie (1969) studied fibres settling in water. It has been shown that, unlike in the Stokes' regime, at Reynolds numbers $Re \sim O(1)$ isolated non-spherical particles tend to exhibit preferential orientation during settling. The same conclusions were drawn by other investigations (Jayaweera and Mason (1965); Feng et al. (1994); Jianzhong et al. (2003)) when studying flows at these Reynolds numbers, in the dilute limit; they have shown that isolated non-spherical particles tend to exhibit preferential orientation during settling.

The torque induced on thin cylinders causes the body to rotate into a stable position with its symmetry axis aligned horizontally. In a relatively recent work Holm et al. (2004) showed that at elevated concentrations, the long range hydrodynamic interactions perturb the flow field to the point where recirculation or swirling like structures are apparent.

In a later work Salmela et al. (2007) conducted a more comprehensive study on the motion of settling particles as a function of concentration, aspect ratio, fluid viscosity, and fibre length for both monodisperse and bi-disperse suspensions and used a similar index of refraction matching tech-

nique. They tracked the motion of tracer fibres in three-dimensions which allowed them to study fibre fractionation in this equipment.

They reported a non-monotonic behaviour in the average settling velocity as a function of concentration with the maximum velocity occurring at a volume fraction of 0.05 % similar to that reported by Herzhaft and Guazzelli (1999). Holm et al. (2004) also observed non-monotonic behaviour with the maximum in the initial settling speed occurring at a crowding number of N $\sim$ 16 for papermaking fibres.

In terms of orientation behaviour, Salmela et al. (2007) showed complex orientation behaviour for suspensions under these conditions. For low concentration they showed that the suspension fibers tend to orient in the horizontal state and then tend to align in the vertical state as concentration increases.

One vital conclusion can be drawn from some unpublished results of Salmela and his coworkers that gives a rise to an understanding of the possibility to fractionate based upon settling. Although not reported in Salmela et al. (2007), they studied the motion of a bi-dispersed suspension comprised of glass rods of two different aspect ratios r=23 and 50 and measured the ensemble-averaged settling velocity of each class of particle.

They measured the settling velocity as a function of the initial suspension

concentration. They found that under dilute conditions each fibre fraction settles at statistically different velocities. This means that there is a possibility for fractionation in this regime. However, with increasing concentration, the differences between the terminal velocities diminish until their difference is indistinguishable and consequently deter the possibility of fractionation in this regime.

In summary, from the above literature, we found that the settling velocity of isolated particles in an unbounded fluid is dependent on density, diameter, orientation and aspect ratio of the cylindrical particles. In the creeping flow regime ($Re \ll 1$) separation of fibers based on difference in settling velocities can be achieved only in extreme dilute suspensions and on condition that the orientation distribution remains constant during descent.

However, at higher concentration for all Reynolds number ranges separation of particles cannot be achieved due to the long range hydrodynamic interactions between particle that leads to floc formation and chaotic swirling structures. Salmela et al. (2007) reported that there is no statistical difference between the settling velocities of particles in bi-disperse suspensions in any reasonable concentrations.

We conclude from above review that particles motion in suspensions with concentration Reynolds number relevant to the industrial suspensions

is extremely complex. Chaotic behaviour is evident due to long range hydrodynamic interactions between particles. This behaviour is observed in the ideal lab situations, when it comes to the real life industrial equipment like cyclones and pressure screens the flow is event more complex being three-dimensional, time-dependent and turbulent in nature.

Now before we move on to discuss particles motion in viscoplastic fluids (where the novel fractionation method is all about) it is a good idea to introduce the difference between Newtonian and non-Newtonian fluids and where viscoplastic fluids stand.

2.3   Non-Newtonian fluids rheology

Fluids are divided to Newtonian and non-Newtonian based on their behavior in the basic shear diagram (shear stress versus shear rate). The Newtonian fluids exhibit a linear relation between shear stress and shear rate with the line passing through the origin.

$$\tau = \mu \gamma \tag{2.2}$$

Where τ is the shear stress, μ is a constant value of dynamic viscosity and γ is the shear rate. A typical example of a Newtonian fluid is water. All other types of fluids are non-Newtonian, meaning that either the relation

between shear stress and shear rate is not linear or the line does not pass through the origin or the material exhibits time-dependent behavior.

Non-Newtonian fluids are divided into several types: shear-thinning fluids, shear-thickening fluids, yield stress (viscoplastic) fluids and time-dependent fluids.

With the shear-thinning fluids, the shear stress - shear rate curve passes through the origin and is concave downwards, with an increase in shear rate resulting in a less than proportional increase in shear stress or in other words the dynamic viscosity is not constant.

For the shear-thickening fluids, the shear stress - shear rate curve also passes through the origin but is concave upwards, meaning that, an increase in shear rate results in a more than proportional increase in shear stress with a variable dynamic viscosity.

For time-dependent fluids, the shear stress versus shear rate data obtained in ascending order of shear rate are different from those obtained in descending order. If the latter is lower, the fluid is called time-dependent shear-thinning (thixotropic), while if the data obtained in descending order is higher, the fluid is called time-dependent shear-thickening (antithixotropic).

In yield stress fluids, the flow may not commence until a threshold value of stress (τ_y, yield stress) is exceeded. A yield stress fluid with shear thinning

behavior is called Herschel-Bulkley fluid, while a yield stress fluid with a linear shear-stress shear rate relation is called Bingham plastic fluid.

To be consistant with related previous studies in the literature, we utilize the Bingham plastic model to describe viscoplastic fluids rheology. The relevant mathematical formulations of Bingham plastic fluids are the constitutive equation and the dimensionless Bingham number defined as follow:

$$\tau = \tau_y + \mu_p \gamma \tag{2.3}$$

$$B = \frac{\tau_y L}{\mu_p V_o} \tag{2.4}$$

where τ is the shear stress, γ the shear rate, μ_p the plastic viscosity, B the Bingham number, L the length scale and V_o the velocity scale. If $\tau < \tau_y$ the Bingham plastic fluid behaves as a solid, otherwise it behaves as a fluid. If $\tau_y = 0$, this model reduces to the Newtonian fluid.

Now since the novel fractionation technique utilizes yield stress fluids as the carrying medium, we need to know how particles behave or move in such a medium. The next section will deal with the motion of particles in yield stress fluids.

2.4 Particle motion in viscoplastic fluids

Particle motion in viscoplastic fluid is more complex than that in Newtonian fluid. If we consider the simplest case of one particle in an unbounded viscoplastic fluid, here the particle has to overcome the force created by the yield stress to start moving. If we denote the net force applied on the particle by F_a , then there should be a critical force value that is required to initiate motion (overcome the fluid yield stress resistive force).

To elaborate more, let us consider an example of a particle immersed in a material having a yield stress τ_y. If F_a is not sufficient to overcome the yield stress then the particle will be suspended indefinitely. Motion will commence when $F_a > \tau_y A_e$, where A_e is the surface area over which the force due to the yield stress is applied. The exact value for A_e however remains an open question. The above relationship can be made dimensionless by scaling each side by a characteristic area of the particle. In this case if we divide each side of the equation by D^2, where D is the diameter of thr particle, we can define a dimensionless force ratio F which represents the criteria for motion:

$$F = \frac{F_a}{\tau_y D^2} > \frac{A_e}{D^2} \tag{2.5}$$

The bound where motion begins is defined as the critical force ratio F_c.

The particle movement depends solely on determination of A_e. Several studies were conducted by researchers to determine A_e, Andres (1961) reported that for spherical particles settling will start when $F_c = 4.8$. Beris et al. (1985) on the other hand suggested that there are two yield surfaces around the spherical particle; a surface with kidney shape away from the sphere and two triangular shapes attached to the leading and trailing edges of the sphere with critical force value of $F_c \sim 11$ to start motion, figure 2.3 .
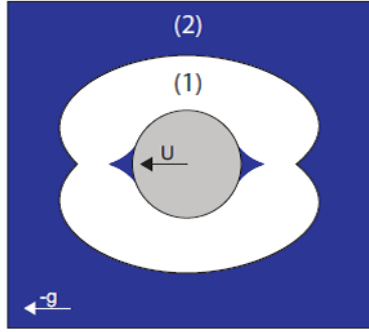
Figure 2.3: Schematic illustrating the yielded (region (1)-white) and unyielded flow regions (region (2)-blue) around a spherical particle in a yield stress fluid, according to the numerical results by Beris et al. (1985). This figure was reproduced from Putz et al. (2008).

Experimentally, Tabuteau et al. (2007); Jossic and Magnin (2001); Laxton and Berg (2005) reported the critical force value for motion in the range $16 < F_c < 25$ and Madani et al. (2010a) in the range $13 < F_c < 29$. In

the same work Madani et al. (2010a) reported F_c for cylinders and bent cylindrical rods oriented in parallel and perpendicul to the direction of the applied centrifugal force in the range of $28 < F_c < 517$ and $87 < F_c < 423$ respectively.

Chhabra (2006) gave a comprehensive summary of settling and sedimentation in different fluids including viscoplastic fluids, he concentrated on terminal velocity and drag coefficients values that are used usually in design purposes for engineering applications. Putz et al. (2008) experimentally estimated the yield surface shape for settling spheres in carbopol solutions by ovoid spheroid that has a major axis dimension of more than 5 times the radius of the sphere.

To summarize, what is clear from this body of work is that during settling the flow is confined in the vicinity of the particle within an envelope the size of which is related to the yield stress of the material. For particles to settle, a critical force must be applied to overcome the resistance created by the yield stress. Relatively little is known about the shape of this surface and the magnitude of the applied force to create motion. What can be said is that the unyielded envelope is larger than the body itself but its shape has yet to be determined rigorously.

With this understanding of particle behaviour in suspensions we are

ready now to introduce the novel fractionation technique developed by Madani et al. (2010b) in the following section.

2.5 The novel fractionation method

In this section, we explain the new particle suspension fractionation method through the work of Madani et al. (2010b). We explore the possible continuous fractionation equipment and the flow associated with it. We introduce the academic problem and state our aim and objectives in this project.

2.5.1 Fractionation principle

By understanding motion of particles in yield stress fluids, we can see that the differences in particles static stability in yield stress fluids when subjected to one applied force make a novel criteria for separation of particles. It is informative at this point to present Madani et al. (2010a,b, 2011)'s results in this regard as they considered two different spherical particles groups of equal dimensions but of different densities.

They rotated each particle in a centrifuge at exactly the same angular velocity and at equal radial positions from the axis of rotation (both particle types experienced the same acceleration field). Particles with greater density, experienced a larger centrifugal force as they have larger mass.

Separation of these two particles types occurs when the centrifugal force applied on type 1 particles, (F_1) is greater than the critical force $(\tau_y A_e)$ and at the same time, this critical force is greater than the centrifugal force applied on type 2 particles, (F_2). Or in other words $F_1 > \tau_y A_e > F_2$.

Figure 2.4 shows the images of suspensions before and after rotation of the centrifuge, the spheres with the higher density are shown in black and that with the smaller density in red. Both sphere types are of same number and distributed evenly throughout the centrifuge.

(a)   (b)
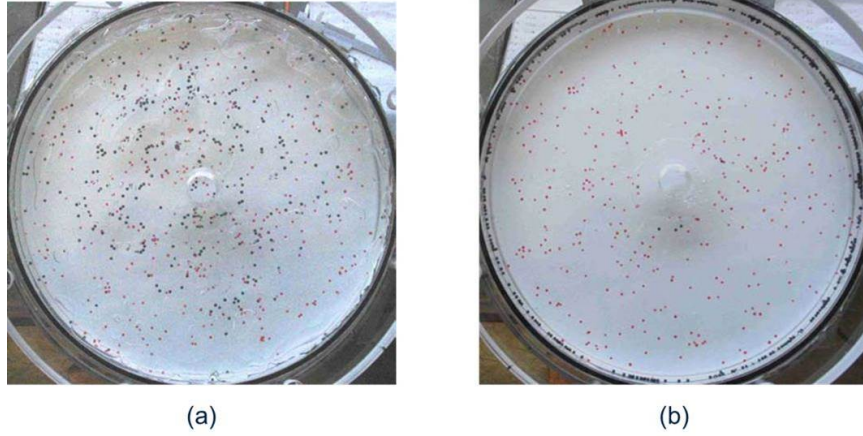
Figure 2.4: A demonstration of the fractionation of a bi-disperse suspension of spherical particles. In (a), an image of the suspension is given before the commencement of the centrifuge. (b) The state of the suspension after the application of the centrifugal force. It should be noted that most of the darker particles are on the periphery of the centrifuge. This figure was reproduced from Madani et al. (2010a).
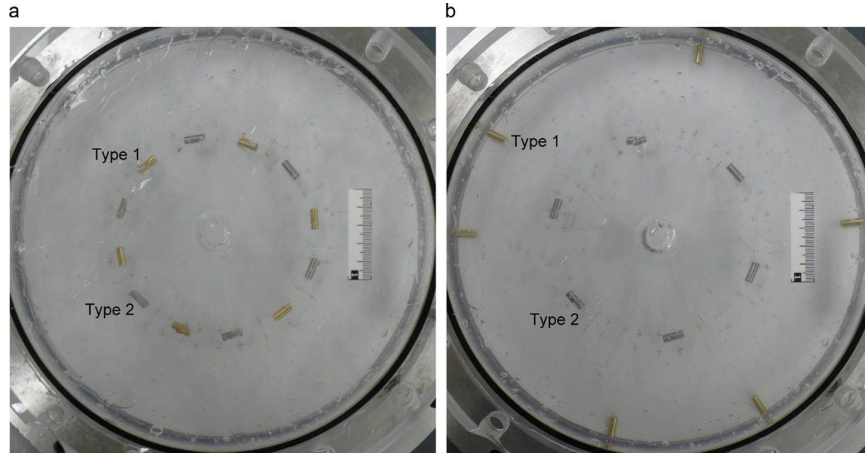
Figure 2.5: A demonstration of the fractionation of a bidisperse suspension of cylindrical particles. In (a) an image of the suspension is given before the commencement of the centrifuge. (b) is the state of the suspension after the application of the centrifugal force. This figure was reproduced from Madani et al. (2010a).

They chose an appropriate rotation rate that led to separation (the lighter particles were statically stable in the suspension while the heavier particles moved to the periphery of the centrifuge).

Similar treatment was done to cylindrical rods as shown in figure 2.5. Here the heavier (type1) rods migrated towards the periphery of the centrifuge under the effect of the centrifugal force while lighter (type2) rods stayed stable. Madani et al. (2011) performed more experiments on papermaking fibre suspensions demonstrating the utility of this approach and has shown that indeed separation may proceed based upon fibre length or

coarseness; their work was however conducted on a batchwise process. The purpose of this work is to advance this technology by demonstrating its potential in an industrially relevant suspension, namely a papermaking suspension.

2.5.2 Development of an efficient continuous fractionation process

Madani et al. (2010b) has introduced a novel continuous fractionation method based upon the principles described earlier. They consider a flow field in which the particles translate in the axial direction which is perpendicular to the motion induced by the centrifugal force. The axial motion is decoupled from the radial (centrifugal) motion. In addition, they emphasise that a significant portion of the flow to be unyielded. To acheive this type of flow, they consider a pressure driven flow imposed onto solid body rotation.

A schematic of the continuous device that uses this method is shown in Figure 2.6. Here particles, suspended in a viscoplastic fluid, are introduced near the inner cylinder (inlet 1) and are transported axially towards the exit; a similar viscoplastic fluid is introduced near the outer cylinder (inlet 2) but no particles are present in this fluid. The walls of each cylinder rotate at the same angular speed and in the same direction. The size of the un-

yielded portion of the flow is controlled by the pressure drop only allowing the operator to control separation and production rates independently. The device has two exits to collect the sorted particles streams.
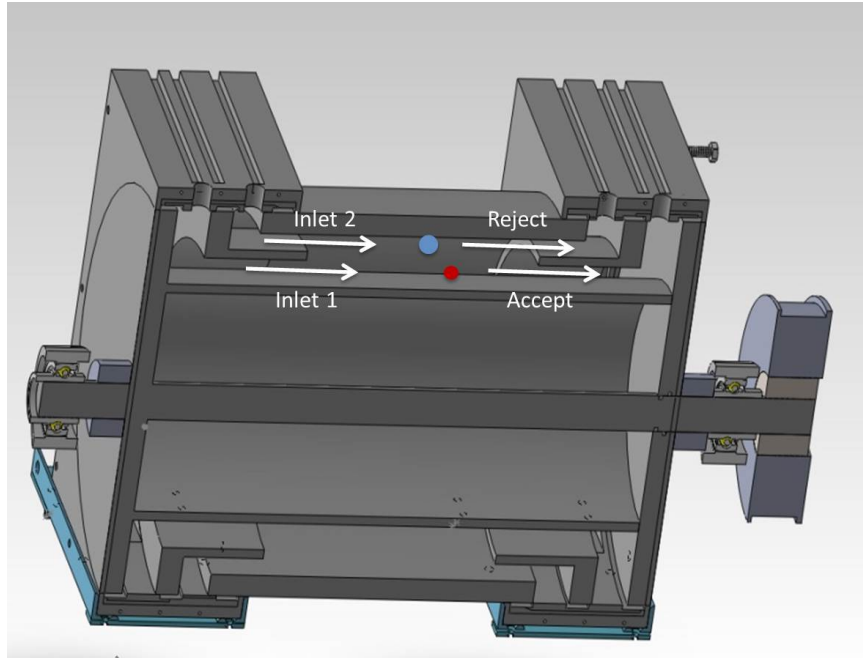
Figure 2.6:   A schematic cross section of the continuous fractionation device.

The entire device rotates and creates a centrifugal field during transport. As described earlier, if an appropriate centrifugal force is selected, a certain fraction of particles will migrate towards the periphery and exit near the outer cylinder. Hence fractionation may occur. To date, the device has yet to be built as more information is required about the details of the flow field.

So basically we have two viscoplastic layers driven by axial pressure drop and rotational angular velocity (solid body rotation), such a flow is referred to as a multi-layer spiral Poiseuille viscoplastic flow.

It is the purpose of this work to develop the design criteria for a stable rotating multi-layer flow. A review of this flow stability will follow in the next section.

2.5.3 Introduction to the academic problem

The flow under consideration is a multi-layer spiral Poiseuille viscoplastic flow in annular geometry that is utilized in the novel fractionation equipment. The most important scientific question in designing such equipment is its flow stability.

In this work we study the stability of the flow using the Bingham plastic model in order to understand the instability bounds due to the presence of different fluids yield stresses, centrifugal forces resulting from rotation and presence of rigid walls containing the flow.

In the Bingham plastic constitutive model the flow may not commence until a threshold value of stress (yield stress) is exceeded. Also, the fluid in this model has a linear shear-stress shear rate relation. So basically this multi-layer flow may have both yielded and un-yielded regions depending on

the local shear stress values compared to each fluid unique yield stress value. Unyielded regions behave like rigid bodies undergoing linear or rotational motion.

We can think of three sources for instability in Poiseuille multi-layer viscoplastic flow. First, is the instability caused by a yielded interface in the event of having yielded velocity profiles of both fluids sharing the interface. Second is the instability caused by Kelvin Helmholtz instability since we have parallel multi-layer flow with different layer velocities.

The third instability may be caused by solid body rotation in the case of density unstable multi-layer flow (having a heavier inner fluid that is closer to the axis of rotation and a lighter outer fluid that is away from the axis of rotation).

To adress the questions associated with these instabilities and the behaviour of the multi-layer annular flow in both the fully developed and entry regions, we review the related literature in four categories: i) non-Newtonian fluid flows in ducts and annular gaps, ii) entrance length, iii) interfacial stability and iv) density current instability.

Now let us start with the first catagory. Solutions of the steady non-Newtonian fluid flow in ducts and annular gaps do exist in the literature for iso-dense cases. Details can be gained from the work of Fredrickson and Bird

(1958); Shul'Man (1970); Grinchik and Kim (1972); Anshus (1974); Hanks (1979); Papanastasiou (1987); Fordham et al. (1991) . Some researchers like Bittleston et al. (2002) and Pelipenko and Frigaard (2004) were interested in displacement viscoplastic flows in annular gaps with emphasis on eccentricity and annulus inclination.

When it comes to introducing wall rotation, Bittleston and Hassager (1992) were one of the first researchers to study viscoplastic fluid flow in ducts with rotation. They investigated the flow in a concentric annulus when there is both axial and tangential flows. The tangent flow arises from the rotation of the inner cylinder of the annulus. They used the Bingham plastic model in their analysis. They solved the flow analytically by considering the flow in a slot and solved the full problem numerically. They found the critical rate at which the inner wall has to move to reduce the plug size to zero.

One of the few research groups that performed an analytical analysis in addition to Bittleston and Hassager (1992) were Liu and Zhu (2010). They studied the axial Couette Poiseuille flow of Bingham fluids through concentric annuli and presented eight different forms of velocity profiles depending on values of three dimensionless parameters: the Bingham, axial Couette numbers and the radius ratio.

Some researchers used the Herschel-bulkley model in their analysis. For

example Nouar (1998) in his work reported the critical wall movement rate to reduce the plug size to zero and Escudier et al. (2002) who used the finite-volume method to solve the flow for the fully developed laminar flow through an eccentric annulus with inner cylinder rotation. Also, Meuric et al. (1998) numerically solved the laminar flow in vertical concentric and eccentric annuli for an imposed axial flow with inner wall rotation. They showed that the inclusion of rotational effects, for a fixed pressure gradient, is likely to increase the axial volumetric flow rate over non-rotating situations in concentric geometries. However, in eccentric annuli, the situation is reversed and the flowrate gradually decreases as the rotation rate is increased.

Some of the researchers like Wang focused on tracking the yield surfaces and mobile plug zones. In his work,Wang (1997) used the finite element method to study Bingham fluid flow in eccentric annuli and in an L-shaped ducts. He found the plug regions and tracked the yield surfaces in these geometries. In a later work,Wang (1998) studied viscoplastic fluid flow in a square duct using a finite-element method and tracked the yield surface and mobile plug zones.

When it comes to studying the linear stability of the flow, insight can be gained from the work of Peng and Zhu (2004) and Madani et al. (2013). Peng and Zhu (2004) studied Bingham-plastic fluid flow between two concentric

cylinders rotating independently and with axial sliding of the inner cylinder (spiral Couette flow). They found that islands of instability, which are found in the spiral Couette flow of Newtonian fluids, may not exist owing to the effect of yield stress. Also they reported that both the rotation of the outer cylinder and a decrease of the gap between the cylinders have stabilizing effects.

Madani et al. (2013) investigated the linear stability of both Newtonian and Bingham fluids in spiral Poiseuille flow in the annular gap between two co-rotating cylinders. They found that solid body rotation increases the margin of stability for both Newtonian and Bingham fluid flow cases. Additionally, the flow is linearly stable for all $B > 0$ where B is Bingham number.

In terms of the shape of axial velocity profiles they found that the steady, fully-developed spiral Poiseuille flow consists of an unyielded region in the center of the channel, for finite B (Bingham number) , bounded by two yielded regions. The position of the yield surfaces was found as part of the solution methodology reported by Liu and Zhu (2010) and is dependent only on B; the swirl component does not affect the position of the plug.

What is clear from this body of literature is that besides previous works there is few, if any, studies we could find in the literature addressing multi-

layer flows in swirl, it is a relatively unexplored area. In related work, the literature is both substantial and protracted for single-fluid viscoplastic flow in annular gaps or in displacement flow, i.e. one fluid contacting another fluid on a plane perpendicular to the axis of motion.

We continue the discussion by considering the entry region solutions in the literature (second category). Perhaps among the first related studies for Newtonian fluid flows are the work of Heaton et al. (1964) who reported the hydrodynamic entry length for different annular geometries. Shortly after that McComas (1967) reported the laminar hydrodynamic entrance length for annular geometries. Shah (1978) explored more geometries including circular and noncircular ducts, parallel plates, rectangular, equilateral triangular, and concentric annular ducts. They proposed a correlation for laminar hydrodynamic entry length for these geometries. After that, Feldman et al. (1982) extended the research to eccentric annular geometries and estimated numerically the hydrodynamic entrance length.

In the most recent studies on Newtonian flows, Durst et al. (2005) estimated the entrance length for pipe flow of both laminar and creeping regimes. Poole and Ridley (2007) modified the Newtonian entrance length correlation proposed by Durst et al. (2005) to be applicable to power law fluids. However, for annular geometries, entrance length was reported only

for higher ranges of laminar regime by researchers like Maia and Gasparetto (2003).

For viscoplastic fluid flows some researchers like (Chen et al. (1970); Shah and Soto (1975); Nowak and Gajdeczko (1983); Vradis et al. (1993); Min et al. (1997)) proposed correlations for the pipe flow enterance length as a constant number times Reynolds number or $(L_e/D_h = CRe)$ in the laminar regime ignoring the lower range of Reynolds number flows where the entrance length collapse to zero based on their correlations. Here, L_e and D_h are the entrance length and hydraulic diameter respectively. This probelm was addressed by Ookawara et al. (2000) and more recently by Poole and Chhabra (2010) who took into consideration the effect of the diffusion dominated (low Reynolds number) pipe flow in their correlations.

The general outcome of the literature in this subject is that the entrance length for annular geometry Newtonian flows is usually shorter than the corresponding ones of pipe flows for the same values of Reynolds numbers. Also, there is little (if any) studies on entry region flows in lower ranges of laminar and creeping regimes of annular flows for both Newtonian and non-Newtonian fluids.

Let us now consider the third cateogry of this literature review, the interfacial stability caused by a yielded velocity profile at the interface. A

considerable amount of literature studies the interfacial instability of multi-layer viscoelastic flows, in contrast, a few researchers like Frigaard (2001), Moyers-Gonzalez et al. (2004) and Huen et al. (2007) studied this instability in multi-layer viscoplastic flows. They reached to a conclusion that a stable multi-layer viscoplastic flow is possible if we are able to preserve an unyielded region at the interface. To do that, the applied shear stress at the interface has to be less than that of the yield stress of one of the fluids that are sharing this interface. So, effectively the velocity profiles are flat for at least one of the fluids sharing the interface.

Now we turn our attention to the last category of the literature review, the problem of density difference between layers. A density current or sometimes called gravity current is usually a horizontal flow in some gravitational field that is driven by a density difference. Due to its wide existence in nature, gravity currents were intensively investigated by researchers.

Let us start with studies involving Newtonian fluids. Benjamin (1968) was one of the first people to study gravity currents mathematically. His studies involved flows of moving heavy fluids with stagnant lighter fluids. Before that, Abbott (1961) and Barr (1967) reported experimental results about intrusions and collisions between fluids of differing density. In an effort to do a comprehensive review of the literature, Simpson published

some work (Simpson (1982), Simpson (1999)) summarizing the research in the field of gravity currents with examples in the atmosphere and in the ocean.

For non-Newtonian flows, the work is substantial and prolonged for power law fluid flows. To mention some, Di Federico et al. (2012), Chowdhury and Testik (2012), Di Federico et al. (2006b), Di Federico et al. (2006a), Longo et al. (2013), Vola et al. (2004), Gratton et al. (1999), Pascal (2003), Longo et al. (2015), Longo et al. (2013) and Ciriello et al. (2015). Their work was related to different studies like gravity currents in a porous layer, creeping gravity currents and propagation of free-surface channelized viscous gravity currents. They consider different geometries like horizontal rectangular tanks, horizontal rigid plane and horizontal rectilinear channels for both steady and unsteady flows.

It is clear that most of the gravity current literature is related to power-law fluids in spreading flows of one fluid over another mostly in horizontal planes or rectilinear channels, etc. To the best of author's knowledge, the problem of density current of two viscoplastic fluids in an annulus with solid body rotation has not been explored previously.

To summarize, studies in the literature are few, if any, for: multi-layer viscoplastic flows with swirl, or annular flows entrance length in lower ranges

of laminar/creeping regimes for both Newtonian and non-Newtonian fluids, and, density current instability in bounded multi-layer flows especially annular flows. In related work the literature is substantial for: single fluid viscoplastic flows/displacement flows, higher ranges of laminar pipe and annular flows, and, density current studies of power law fluids spreading flows in planes or rectilinear channels. For interfacial stability, a stable multi-layer viscoplastic flow is possible if we maintain at least one velocity profile of the fluids sharing the interface to be flat.

Based on this summary of the literature, our aim is to investigate the multi-layer spiral Poiseuille viscoplastic fluid flow in annuli. We vary the rheology of the fluid spatially in cross stream direction in order to allow us study the layered annular flows. We explore the entrance length for both Newtonian and viscoplastic fluids in lower ranges of laminar and creeping regime. In addition we explore the effect of density difference between layers.

At this point let us define the objectives of this research. Our main goal is to design a continuous fractionation equipment that employs the novel fractionation method. To acheive this goal, we need to fulfill the following objectives:

- To understand the stability of a multi-layer annular flows in which the viscoplastic fluids are of different rheology. Here we will analyze

the stability of two fluids in contact, in swirling Poiseuille flow. We solve analytically the fully developed problem of the Spiral Poiseuille multi-layer flow for stability of the flow in the interface area.

- We will examine computationally (in a labrotary device using 2D axisymmetric CFD simulation) the full annulus problem including estimating the entrance length of the flow to predict the required axial length of the fractionation device. In this simulation we will examine the effect of the design and elongational stresses in the entry region, on final interface position. In addition, we will explore the effect of density current and Kelvin-Helmholtz instabilities on the flow stability. We will benchmark this computational solution with the fully developed analytical solution.

- Study computationally the continuous fractionation device including the inlet and exit conditions. We will simulate the flow field in a laboratory device using 2D axisymmetric CFD simulation. We will compare the computational solution of the flow in the device with the fully developed analytical solution.

There are some limitations to our analysis as this work is intended to provide the theoretical basis to apply the novel fractionation principle on

continuous industrial applications and to provide a design for the fractionation device. Additional experimental work is needed to validate the operation and the efficiency of this new principle in a physical fractionation process.

The first limitation is that we do not consider chemical reactions between fluid layers. As an example the fractionation efficiency in fluids with different pH concentration need to be explored experimentally. In this work we assume no chemical reactions between fluid layers.

The second limitation is that we do not consider diffusion between layers due to particle movement between layers. As discussed earlier, the effect of solid particles on the flow is limited to a small envelope surrounding the particle especially in the laminar regime under consideration which has typically a very large Peclet number. For large Peclet number, the diffusive effects are usually expected to be limited over the simulations time scales.

Chapter 3

The fully developed problem and particle fractionation

We consider the fully developed fluid flow in an annular space formed between an inner and outer cylinders of radii $\hat{r} \in [\kappa\hat{R}, \hat{R}]$, where κ is a constant defined in the interval $(0, 1)$, figure 3.1. In this work we define the hatted notation to represent a dimensional quantity.
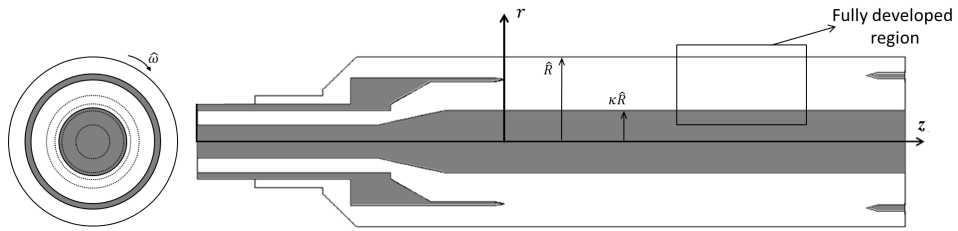
Figure 3.1:   A schematic of the model geometry.

The inner and outer cylinders rotate with the same angular speed $\hat{\omega}$. The

flow is subjected to a constant pressure gradient $\hat{G}$, in the axial direction. We consider a multi-layer flow where two or more fluids flow with their interface aligned parallel to the direction of flow.

Each individual fluid has its unique physical and rheological properties. To be consistent with the work of Bittleston and Hassager (1992) and Madani et al. (2013) that considered a single viscoplastic fluid, we utilize the Bingham plastic rheological model to describe multi-layer fluids rheology with the apparent viscosity $\hat{\mu}^{(k)}$ and yield stress $\hat{\tau}_y^{(k)}$ defined for each fluid, where $k = 1, 2, 3...etc$. The fluids are incompressible with the same density $\hat{\rho}$.

The location of each layer is defined apriori by the position of its upper boundary $\hat{r}_l^{(k)}$. Hence each layer is defined in the region $(\hat{r}_l^{(k-1)}, \hat{r}_l^{(k)})$. For simplicity in the analysis we will drop the superscript and assume that these properties vary as a function of radial position.

To develop an appropriate model for the problem, we assume the flow to be laminar, steady, and axisymetric, the fluids to be Non-Newtonian (viscoplastic) with constant properties. In addition, we assume no chemical reactions and the wall surfaces to be smooth and free from active impurities.

The flow in the previously described geometry is governed by the basic partial differential equations which result from the consideration of both the

conservation of mass principle (continuity equation) and the conservation of momentum principle (Navier-Stokes equations). These equations are given below for laminar, steady and incompressable flow.

$$\nabla.\hat{\mathbf{u}} = 0 \tag{3.1}$$

$$\hat{\rho}(\hat{\mathbf{u}}.\nabla)\,\hat{\mathbf{u}} = -\nabla\hat{p} + \nabla.\hat{\boldsymbol{\tau}} \tag{3.2}$$

where $\hat{\mathbf{u}}$ is the velocity, $\hat{p}$ the pressure and $\hat{\boldsymbol{\tau}}$ the deviatoric stress tensor. we non-dimensionalize the Navier-Stokes equations using a length scale of $\hat{R}$ and a viscosity scale of $\hat{\mu}^{(1)}$. We define a velocity scale $\hat{U}_o$, time scale $\hat{t}_o$ and pressure scale $\hat{\tau}_c$ of :

$$\hat{U}_o = \sqrt{(\kappa\hat{\omega}\hat{R})^2 + \left(\frac{\hat{G}\hat{R}^2}{\hat{\mu}^{(1)}}\right)^2} \tag{3.3}$$

$$\hat{t}_o = \frac{\hat{\rho}\hat{R}^2}{\hat{\mu}^{(1)}} \tag{3.4}$$

$$\hat{\tau}_c = \frac{\hat{\mu}^{(1)}\hat{U}_o}{\hat{R}} \tag{3.5}$$

Where $\hat{G}$ is the pressure drop per unit length. In the definition of $\hat{U}_o$, the two terms reflect the effect of rotational speed $\hat{\omega}$ and pressure drop rate

$\hat{G}$ on the flow cheracteristics.

Using these scalings, and omitting the hat notation for dimensionless variables, the scaled constitutive equations for the fluid are:

$$
\begin{cases}
\tau_{ij} = \left(\mu(r) + \frac{B(r)}{\dot{\gamma}} \right) \dot{\gamma}_{ij} \Leftrightarrow \tau > B(r) \\
\dot{\gamma}_{ij} = 0 \Leftrightarrow \tau \le B(r)
\end{cases}
\tag{3.6}
$$

Where $\dot{\gamma}$ and τ are the rate of strain and stress tensors, respectively and B is Bingham number. These are defined by:

$$
\dot{\gamma} = \left(\sum \frac{1}{2} \dot{\gamma}_{ij} \dot{\gamma}_{ij} \right)^{\frac{1}{2}}
\tag{3.7}
$$

$$
\tau = \left(\sum \frac{1}{2} \tau_{ij} \tau_{ij} \right)^{\frac{1}{2}}
\tag{3.8}
$$

where

$$
\dot{\gamma}_{ij} = \nabla (u_{ij} + u_{ji})
\tag{3.9}
$$

With these, we find that this flow is characterized by five dimensionless groups, the axial and tangential Reynolds numbers, Re_z and Re_θ, the Bingham number , B, the ratio of the swirl and axial velocities, ω, and the ratio of the radii of the two cylinders, κ defined as :

$$Re_z = \frac{\hat{\rho}\hat{U}_o\hat{R}}{\hat{\mu}^{(1)}}$$

$$Re_\theta = \frac{\hat{\rho}\hat{\omega}\hat{R}^2}{\hat{\mu}^{(1)}}$$

$$B(r) = \frac{\hat{\tau}_y(r)\hat{R}}{\hat{\mu}^{(1)}\hat{U}_o}$$

$$\omega = \frac{Re_\theta}{Re_z}$$

$$\kappa = \frac{\hat{R}_i}{\hat{R}}$$

where $\hat{R}_i$ is the inner radius of the annulus.

If fully developed, the equations of motion reduce to:

$$\frac{1}{r}\frac{du_\theta}{d\theta} + \frac{du_z}{dz} = 0 \tag{3.10}$$

$$\frac{d}{dr}(r^2\tau_{r\theta}) = 0 \tag{3.11}$$

$$\frac{1}{r}\frac{d}{dr}(r\tau_{rz}) = G \tag{3.12}$$

with

$$\dot{\gamma} = \frac{1}{\sqrt{2}}\left(\dot{\gamma}_{r\theta}^2 + \dot{\gamma}_{rz}^2\right)^{\frac{1}{2}} \tag{3.13}$$

$$\tau = \frac{1}{\sqrt{2}}\left(\tau_{r\theta}^2 + \tau_{rz}^2\right)^{\frac{1}{2}} \tag{3.14}$$

$$\dot{\gamma}_{r\theta} = r\frac{d}{dr}\left(\frac{u_\theta}{r}\right) \tag{3.15}$$

$$\dot{\gamma}_{rz} = \frac{d}{dr}\left(u_z\right) \tag{3.16}$$

Integrating the governing equations 3.11 and 3.12 leads to:

$$\tau_{r\theta} = \frac{C_1}{r^2} \tag{3.17}$$

$$\tau_{rz} = \frac{Gr}{2} + \frac{C_2}{r} \tag{3.18}$$

To advance, we need to eliminate $\dot{\gamma}$. To do so, we first square the stress-strain relationship. i.e.

$$\begin{cases} \tau_{ij}^2 = \left(\mu(r) + \frac{B(r)}{\dot{\gamma}}\right)^2 \dot{\gamma}_{ij}^2 \Leftrightarrow \tau > B(r) \\ \dot{\gamma}_{ij}^2 = 0 \Leftrightarrow \tau \le B(r) \end{cases} \tag{3.19}$$

And then summing the terms,

$$\begin{cases} \sum \tau_{ij}^2 = \left(\mu(r) + \frac{B(r)}{\dot{\gamma}}\right)^2 \sum \dot{\gamma}_{ij}^2 \Leftrightarrow \tau > B(r) \\ \sum \dot{\gamma}_{ij}^2 = 0 \Leftrightarrow \tau \le B(r) \end{cases} \tag{3.20}$$

Or

$$
\begin{cases}
\dot{\gamma} = \frac{\tau - B(r)}{\mu(r)} \Leftrightarrow \tau > B(r) \\[4mm]
\dot{\gamma}^2 = 0 \Leftrightarrow \tau \leq B(r)
\end{cases}
\tag{3.21}
$$

Substituting equations 3.15, 3.16, 3.17 and 3.18 into equation 3.21 yields the final system of equations:

$$
\frac{d}{dr}\left(\frac{u_\theta}{r}\right) = \frac{C_1}{r^3}\frac{1}{\mu(r)}\left(1 - \frac{B(r)}{\tau}\right) \Leftrightarrow \tau > B(r)
\tag{3.22}
$$

$$
\frac{d}{dr}\left(u_z\right) = \left(\frac{Gr}{2} + \frac{C_2}{r}\right)\frac{1}{\mu(r)}\left(1 - \frac{B(r)}{\tau}\right) \Leftrightarrow \tau > B(r)
\tag{3.23}
$$

The governing Equations are subject to the following boundary conditions including the walls non-slip conditions:

- At interface:

$$
r = r_i
$$

- A per unit length pressure drop across the annulus of:

$$
\hat{G}
$$

- At the inner wall:

$$u_z(\kappa) = 0$$

$$u_\theta(\kappa) = \frac{\kappa \hat{\omega} \hat{R}}{\hat{U}_o}$$

- At the outer wall:

$$u_z(1) = 0$$

$$u_\theta(1) = \frac{\hat{\omega} \hat{R}}{\hat{U}_o}$$

3.1 Method of solution

Here, the final system of equations together with the boundary conditions forms a boundary value problem. The equations are integrated and solved using Matlab built-in program bvp4c. The program bvp4c uses a collocation method that results in a system of nonlinear algebraic equations that is solved by a variant of Newtons method. This involves many partial derivatives of several kinds. To make solving BVPs as easy as possible, the program approximates these partial derivatives with finite differences, Shampine et al. (2005).

3.2   Validation

We compare the present model with the work of Madani et al. (2013) for single viscoplastic fluid in a concentric annulus of 0.8 radius ratio. Validation is carried out for two values of Bingham number, $B = 0.5$ and 0.3.

Figure 3.2 shows the calculated dimensionless axial velocity profile compared to Madani et al. (2013) values. The agreement is very good with the mean percentage difference falls below 1.5%.
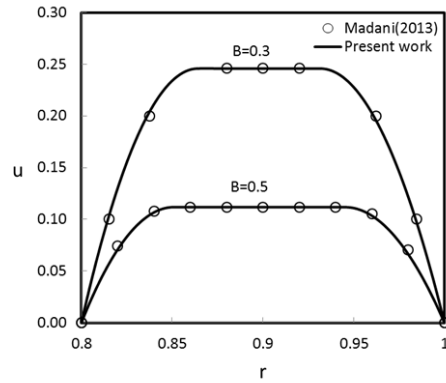
Figure 3.2:   Dimensionless axial velocity profile comparison between present work and the work of Madani et al. (2013).

3.3 Stability definition

As highlighted earlier, a stable multi-layer viscoplastic flow is possible if the applied shear stress at the interface is less than that of the yield stress of one of the fluids that are sharing this interface, (Frigaard (2001); Moyers-Gonzalez et al. (2004); Huen et al. (2007)). Having the applied shear stress below the yield stress means that the fluid will not deform and we will have plug flow. This plug area is needed for the fractionated particles to penetrate through in order to be separated from other particles in the suspension.

Here the force required for the targeted particles (of certain geometry and density) to pass the plug region is known because we know the fluid yield stress value that we need to overcome. But in the yielded region of the flow on the other hand the applied stress on fluid is more than the yield stress and all particles of different densities and geometries move with the flow.

Based on the above definition of stability, the flow will be divided to the following sub-categories with regard to stability:

- An unstable flow where the applied shear stress on both fluids at the interface is higher than the yield stress of each fluid. Here, both fluids are yielded at the interface, figure 3.3-a.

- A stable flow. In this type, the applied shear stress at one or more of the two fluids in the interface is lower than its yield stress value. This situation makes the flow un-yielded on at least one side of the interface. If the flow is un-yielded in the inner fluid region, we denote the flow as inner stable flow, figure 3.3-b and if the flow is un-yielded on the outer fluid region, we would call it an outer stable flow, figures 3.3-c.

3.4 Results

We study the effect of the yield stress, plastic viscosity and radius ratio numbers defined respectively as follows:

$$\tau_y^{(r)} = \frac{\hat{\tau}_y^{(r)}}{\hat{\tau}_y^{(1)}}$$

$$\mu^{(r)} = \frac{\hat{\mu}^{(r)}}{\hat{\mu}^{(1)}}$$

$$\kappa = \frac{\hat{R}_i}{\hat{R}}$$

where $\hat{R}_i$ is the inner radius of the annulus.

The inner and outer fluids flow rates are defined respectively as:
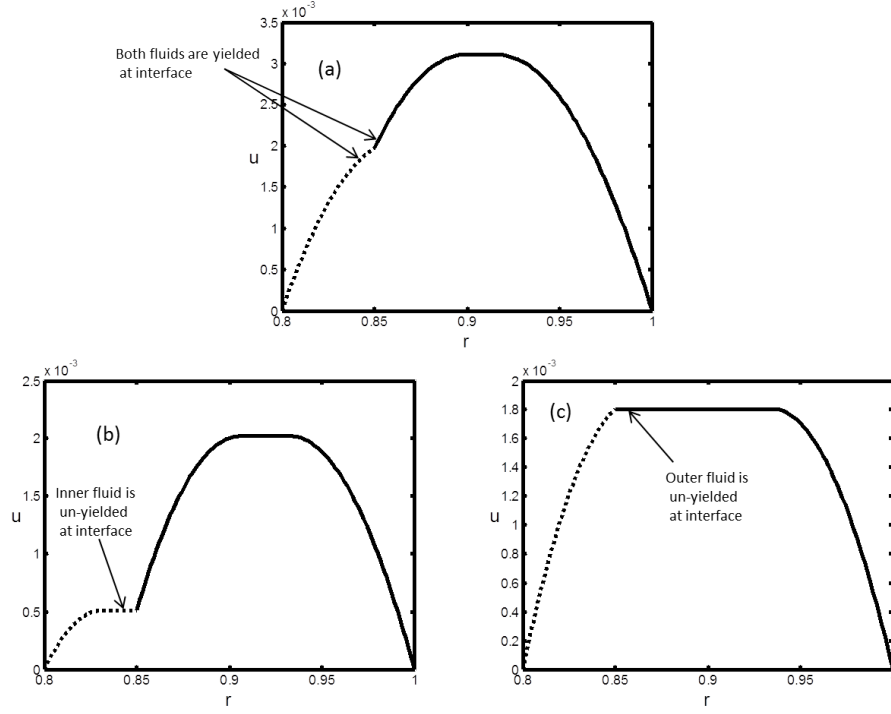
Figure 3.3: Multi-layer flow stability categories: (a) an unstable flow, (b) an inner stable flow and (c) an outer stable flow. The dashed lines are for the inner fluid velocity profiles.

$$Q_1 = \frac{\hat{Q}_1}{\hat{Q}_o}$$

$$Q_2 = \frac{\hat{Q}_2}{\hat{Q}_o}$$

Where $\hat{Q}_1$ and $\hat{Q}_2$ are the dimensional inner and outer fluids flow rates.

$\hat{Q}_o$ is the reference flow rate defined using the annulus cross-sectional area

Series	$\tau_y^{(1)}$	$\tau_y^{(2)}$	$\mu^{(1)}$	$\mu^{(2)}$	κ
1	(0,1,2)	0.5	0.75	0.75	0.6
2	1	(0,0.5,2)	0.75	0.75	0.6
3	1	0.5	(0.375,0.75,1.5)	0.75	0.6
4	1	0.5	0.75	(0.375,0.75,1.5)	0.6
5	1	0.5	0.75	0.75	(0.6,0.8,0.9)

Table 3.1: A summary of the runs conditions simulated for each parameter: inner and outer fluids yield stresses, plastic viscosities and radius ratio.

$\hat{A}_c$ and the reference speed $\hat{U}_o$:

$$\hat{Q}_o = \hat{A}_c\hat{U}_o$$

The standard case has the following parameter values:

$$\tau_y^{(1)} = 1, \tau_y^{(2)} = 0.5, \mu^{(1)} = 0.75, \mu^{(2)} = 0.75, \kappa = 0.6$$

The detailed runs conditions are shown in Table 3.1.

One representative case is shown ,i.e. series 1 as defined in the table 3.1, in figure 3.4. This figure outlines the flow state (contour) and defines the pressure drop and interface position at different inlet flow rate conditions. What is clear in this image is that stable flows are achievable and the region

of stability grows with increasing yield stress.

Similar results can be found for the other cases considered (which are shown in Appendix A). Our findings can be summarized into a number of qualitative "rules of thumb"

(a) Increasing yield stress increases the region of stability while increasing the pressure drop required to maintain the desired flow rate.

(b) The size of the stability window was fairly insensitive to the viscosity ratio or channel size.

At this point we turn our attention to attempting to use these results to estimate if separation is possible, given a stable flow field. We represent this methodology as a toy problem to outline the key features required to make such an estimate. This discussion is by no-means a complete analysis.

For separation to occur in the annulus, we need to know the difference in start criteria, as given in figure 3.5, as an example, and the settling rate of the particle introduced on the inner radius. The settling rate and the gap size represent the settling time in the mixing zone which must be less than the residence time in the device, figure 3.6.

As such we built a small algorithm to study the potential combination of operating conditions to separate two particles for a given rheology of fluids. Formally we seek a solution for the rotational rate and flowrates to separate

particles in a known viscoplastic fluid, subject to the interface being stable and the settling time being smaller than the residence time. The settling rate of particles in a viscoplastic fluid where obtained from Derksen et al. (2011).

The test case which we will discuss is similar to what we will conduct on the laboratory device. Here, we will attempt to determine the flowrates to separate a 2.5 mm steel spheres from a dilute suspension of spheres with smaller diameter.

The spheres are suspended in a fluid with a yield stress of 1 Pa and is layered onto another fluid with a yield stress of 0.5 Pa. The first step in this analysis is to define the critical rotation rate to cause motion. We examine the data from Madani and define the critical rotation rate, i.e.

$$\omega_c > \sqrt{F_c \frac{\tau_y D^2}{\Delta \rho V R}}$$

where F_c is the critical force as determined by Madani et al. (2010a) for different particle sizes. $\Delta \rho$ is the difference between particle and suspension densities, V is the volume of the spherical particle, R is the distance between the particle and axis of rotation, τ_y is the suspension yield stress and D is the particle diameter.

With this we solve equations 3.22-3.23, for the given fluid, and attempt
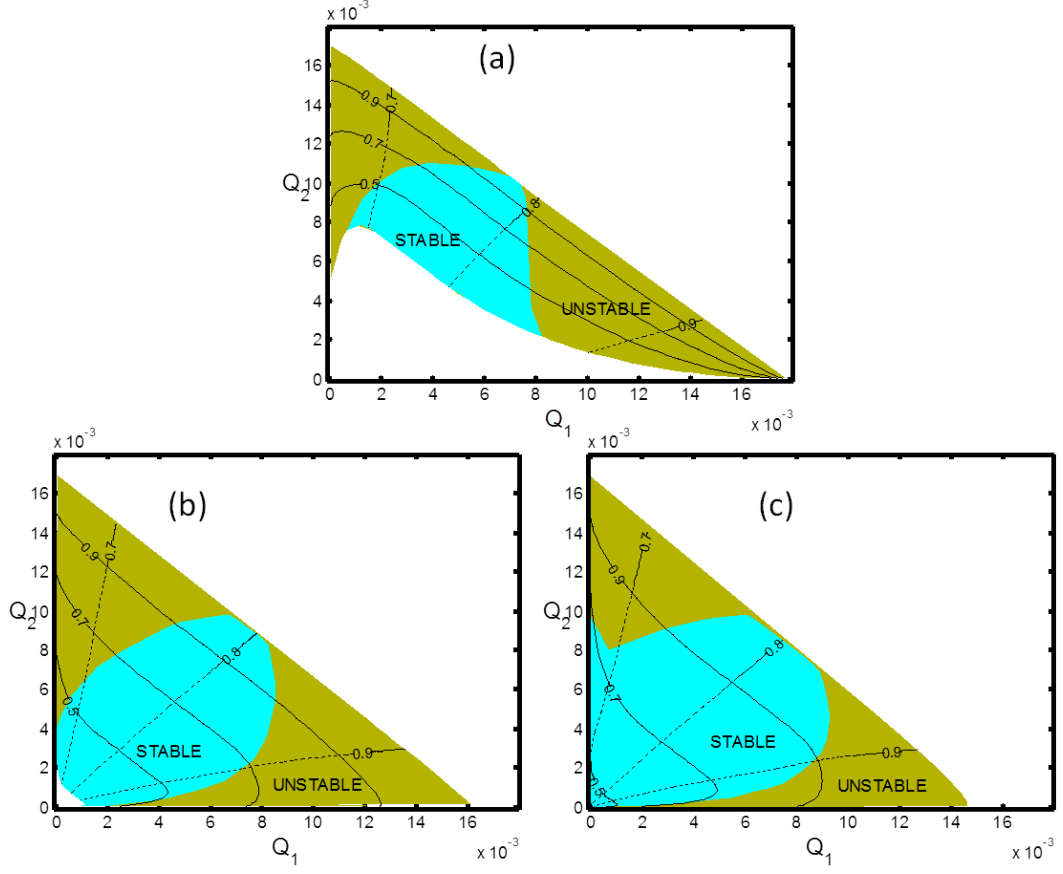
Figure 3.4: The solution of equations 3.22-3.23 for the conditions given as series 1 in table 3.1. The colour map defines the stability of the flow state, as given in figure 3.3. The dashed lines represent the interface position and the solid lines represent the pressure drop rate: (a) $\tau_y^{(1)} = 0$, (b) $\tau_y^{(1)} = 1$, (c) $\tau_y^{(1)} = 2$.
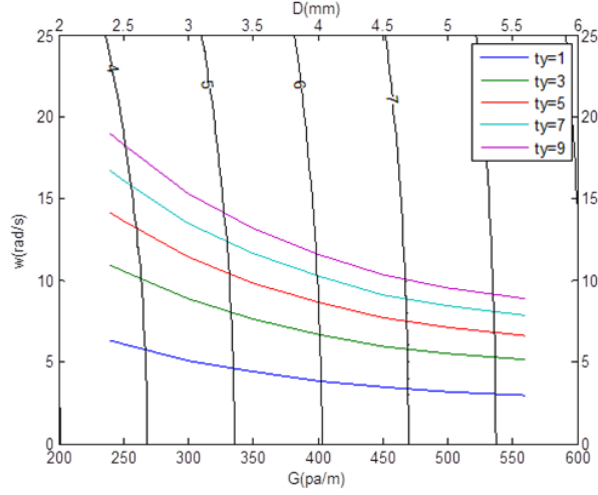
Figure 3.5: Fractionation curves for spherical stainless steel particles in different yield stress fluids. The critical rotational speeds ω are denoted by the colored lines and the black lines for the characteristic speed U_c. Radius ratio, $\kappa = 0.6$, outer radius, $R = 0.127$ m, plastic viscosity, $\mu = 1.0833$ $Pa.s$, spheres density, $\rho_s = 7800$ kg/m^3 and suspension density, $\rho_f = 1000$ kg/m^3.

to find the subset of cases in which the settling time is smaller than the residence time in a stable operating window. The results are shown in figure 3.7. The blue lines in this case represent the ratio of residence to settling times. When this ratio is greater than unity, we consider this to be an acceptable solution.

A number of potential flow configurations are evident (stable, unstable and operating window). The operating window configuration is defined as a stable flow with at least 50% of the inner fluid region being unyielded.
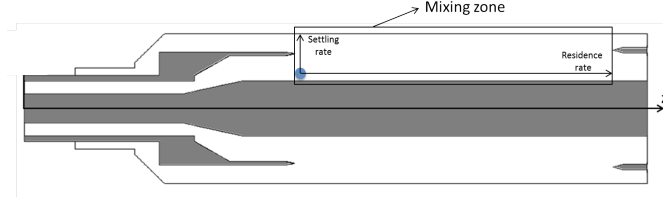
Figure 3.6: Settling and residence rates in the mixing zone of the device.

If the inner fluid is mostly yielded, then there will be no enough space for the targeted particles to penetrate through to the other layer and achieve separation. In addition, the flow will be at risk of losing its stability.

In this chapter we solve analytically the fully developed region of the flow of interest. We validate the solution against previous single fluid viscoplastic analytical work. We categorize the stability of the flow based on the yielding condition of the fluids sharing the interface. We present the effect of fluids rheology on the flow stability.

In addition, we show that the novel fractionation method can be used effectively to fractionate particles suspensions in continuous mode. We provide some useful curves and diagrams that characterise the flow with regards to its stability and its ability to successfully fractionate particles suspensions. To do so, we define the fractionation operating window, we present the critical rotational speed to fractionate particles of different sizes in fluids of variable yield stress values.
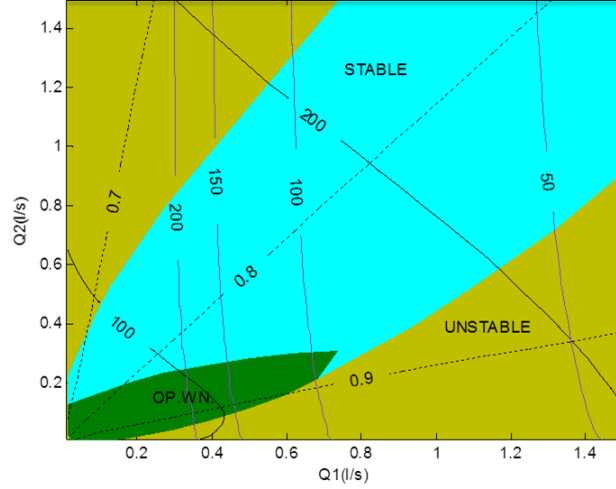
Figure 3.7: Flow stability and operating diagram. Residence to settling time ratio in blue lines, interface locations in black dashed lines and dimensionless pressure drop rate in solid black lines. The annulus axial length $L = 50\ cm$, inner fluid yield stress $\tau_y^{(1)} = 1\ Pa$, outer fluid yield stress $\tau_y^{(2)} = 0.5\ Pa$, radius ratio, $\kappa = 0.6$, outer radius, $R = 0.127\ m$, plastic viscosity, $\mu^{(1)} = \mu^{(2)} = 0.75\ Pa.s$, spheres density, $\rho_s = 7800\ kg/m^3$ and suspension density, $\rho_f = 1000\ kg/m^3$, $\omega = 37.2\ rad/s$ and pressure drop rate of $(50-500)\ Pa.s$.

Moreover, we develop a flow and stability diagram for a specific fractionation case (known inner and outer fluids rheology, annulus geometry and targeted particles size and density). In this diagram we show the areas of stability, instability, operating window and other useful information to the operator.

55

Chapter 4

The full annulus problem

and density current effects

In the previous chapter we examined the fully developed solution of the problem in order to have the first base for designing the continuous device. The second base will be solving the entrance region of the multi-layer viscoplastic flow inside an annulus. This intermediate stage is needed primarily to design the mixing point of the continuous device. In addition to our treatment of the yielded interface instability in the previous chapter, we extend the discussion to the Kelvin Helmholtz and density current instabilities in our effort to address all aspects of the flow stability.

In this chapter, we aim at obtaining a numerical solution for the full system of Navier stokes equations of the pressure driven laminar forced multi-layer flow problem of an annulus with rotating walls of a constant angular velocity. The layers are of viscoplastic fluids with variable density

and are aligned in parallel to the annulus axis.

4.1 Mathematical modeling

We consider the fluid flow in the annular space formed between an inner and outer cylinders of radii $\hat{r} \in [\kappa\hat{R}, \hat{R}]$, where κ is a constant defined in the interval $(0,1)$, figure 4.1. In this work we define the hatted notation to represent a dimensional quantity.
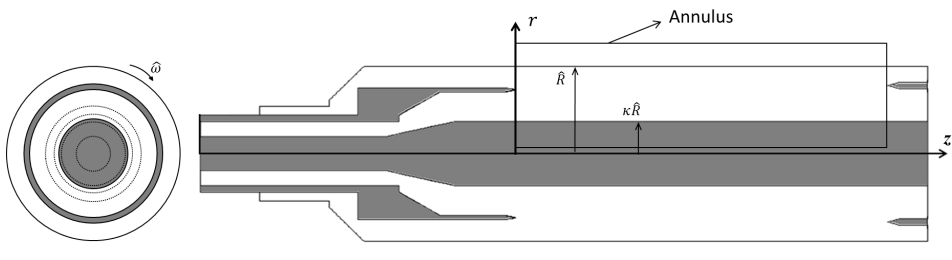
Figure 4.1:   A schematic of the model geometry.

The inner and outer cylinders rotate with the same angular speed $\hat{\omega}$. The flow is subjected to a constant pressure gradient $\hat{G}$, in the axial direction. We consider a multi-layer flow where two fluids flow with their interface aligned parallel to the direction of flow.

We follow the same mathematical modeling as highlighted in chapter three taking into consideration that k is limited to $k = 1, 2$ since we have

57

only two fluids. Here, 1 denotes the inner fluid and 2 denotes the outer fluid. Both the inner and outer fluids enter the annulus with a uniform velocity profile. In developing our model we assume the same assumptions as we did in the previous study with the exception of the fully developed flow assumption.

We utilize the concentration α_1 to model the change in concentration between pure fluids 1 and 2 with $\alpha_1 \in (0,1)$. After scaling , the non-dimensional continuity and Navier-Stokes equations are

$$\nabla.\mathbf{u} = 0 \tag{4.1}$$

$$(1 + \phi At) \, Re_z (\mathbf{u}.\nabla) \, \mathbf{u} = -\nabla p + \nabla.\boldsymbol{\tau} \tag{4.2}$$

where $\mathbf{u}$ is the velocity, p the pressure and $\boldsymbol{\tau}$ the deviatoric stress tensor.

Here the function $\phi(\alpha_1) = 1 - 2\alpha_1$ has the range of $\phi \in (-1,1)$ for $\alpha_1 \in (0,1)$. The additional dimensionless parameter is the Atwood number, At which results from the variable density nature of the model. The Atwood number is defined as

$$At = \frac{\rho_1 - \rho_2}{\rho_1 + \rho_2}$$

58

where, ρ_1 and ρ_2 are the densities of the heavier and lighter fluids, respectively.

It is imperative at this point to define the Richardson number since we will explore the Kelvin Helmholtz instability of the flow. The Richardson number (Ri) is the dimensionless number that expresses the ratio of the buoyancy term to the flow gradient term.

$$Ri = \frac{\text{buoyancy term}}{\text{flow gradient term}} = \frac{g}{\rho} \frac{\nabla \rho}{(\nabla u)^2}$$

where g , ρ and u are acceleration of gravity, density and velocity, respectively.

In the current numerical solution, all control volumes are filled with one or more of the phases (fluids). The κth fluids volume fraction in a control volume is called α_κ and we can have $\alpha_\kappa = 0$ if the control volume is empty of the κth fluid, $\alpha_\kappa = 1$ if the control volume is full of the κth fluid and $0 < \alpha_\kappa < 1$ if the control volume contains an interface between the κth fluid and other fluids. Here, in each control volume, the volume fractions of all phases sum to unity.

$$\sum_{\kappa=1}^{n} \alpha_\kappa = 1 \tag{4.3}$$

Where n is the number of phases.

All properties appearing in the continuity and momentum equations are volume fraction averaged properties. For example, the volume fraction averaged density is computed as follows

$$\rho = \sum_{\kappa=1}^{n} \rho^{(\kappa)} \alpha_\kappa \tag{4.4}$$

The governing equations are subject to the following inlet, outlet and non-slip boundary conditions:

- At the inlet (z = 0):

  A uniform velocity profile is used for the z-component of the fluids velocity

  $$u_{z1} = \frac{u_{o1}}{\hat{U}_o}$$

  $$u_{z2} = \frac{u_{o2}}{\hat{U}_o}$$

  while the r and θ components of the velocity are assumed to be zero.

- At the outlet (z = L):

  We impose zero axial gradients at the outlet (outflow condition in fluent).

- At the inner wall, we impose the non-slip condition:

$$u_z(\kappa) = 0$$

$$u_\theta(\kappa) = \frac{\kappa \hat{\omega} \hat{R}}{\hat{U}_o}$$

- At the outer wall, we impose the non-slip condition:

$$u_z(1) = 0$$

$$u_\theta(1) = \frac{\hat{\omega} \hat{R}}{\hat{U}_o}$$

We conduct different experiments to study the hydrodynamic entrance length. Here we include reference to the Reynolds number based on the hydraulic diameter and average velocity, Re_h, to compare the current results with previous literature work. Re_h is defined as

$$Re_h = \frac{\hat{\rho}^{(1)} \hat{V}_{av} \hat{D}_h}{\hat{\mu}^{(1)}}$$

where $\hat{V}_{av}$ is the flow average velocity and $\hat{D}_h$ is the annulus hydraulic diameter. Details of entrance length study runs conditions are shown in table 4.1. Another set of runs are conducted to study the interface behaviour, density current instability and Kelvin Helmholtz instability. These runs conditions are detailed in table 4.2.

Study	Re_h	Re_z	$B^{(1)}$
	0.10	8.1×10^1	0.000
	1.00	8.1×10^2	0.000
Newtonian	10.00	8.1×10^3	0.000
	72.00	5.8×10^4	0.000
	100.00	8.1×10^4	0.000
	200.00	1.6×10^5	0.000
	0.10	5.4×10^2	0.047
Viscoplastic	1.00	1.3×10^3	0.019
	10.00	8.7×10^3	0.003

Table 4.1: A summary of the runs conditions simulated for the entrance length study. Simulations are for single fluid of Newtonian or viscoplastic behaviour.

Study	Re_z	Re_θ	At	$B^{(1)}$	$B^{(2)}$
Interface behaviour	$4.4 \text{ x } 10^2$	8.70	0.00	0.058	0.035
	$8.2 \text{ x } 10^2$	8.70	0.00	0.031	0.019
	$4 \text{ x } 10^2$	0.00	0.20	0.00	0.00
Density current instability	$4.2 \text{ x } 10^2$	166.00	0.20	0.00	0.00
	$2 \text{ x } 10^4$	166.00	0.20	0.062	0.062
	$3 \text{ x } 10^4$	166.00	0.20	0.064	0.064
Kelvin Helmholtz Instability	$5.2 \text{ x } 10^3$	7.25	0.05	0.000	0.000

Table 4.2: A summary of the runs conditions simulated for each study: Interface behaviour, Density current and Kelvin Helmoholtz instabilities.

4.2   Method of solution

For this case we have to solve the flow in the entire annulus including the entry region. This means that we have to deal with the full form of the governing equations, there is no analytical means to solve the governing equations and hence they will be treated numerically.

We solve the governing equations of the conservation of mass and momentum using a finite difference technique. A numerical algorithm will be used to solve for the three velocity components and pressure of the solution domain. The problem under consideration is an axi-symmetric steady laminar problem; the governing equations are solved numerically using the FLUENT software. The numerical model uses a control-volume-based technique to convert the governing equations to algebraic equations that can be solved simultaneously.

This control volume technique is based on discretizing the domain into discrete control volumes using a computational grid. Then integrating the governing equations about each control volume, yielding discrete equations that conserve each quantity on a control-volume basis. After that the discretized equations are linearized. The resultant linear equation system is solved to yield updated values of the dependent variables.

The differencing schemes used are both formally second-order in ac-

curacy: central differencing is used for the diffusive terms and a second-order up-winding scheme for the convective terms. Coupling of the pressure and velocity was achieved using the well-known semi-implicit method for pressure-linked equations (SIMPLE) implementation of Patankar (1980).

4.3 Grid independence test

To achieve grid independence, the solution was computed for different grid sizes to assess the effects of mesh refinement. The grid sizes used were 100x266, 150x400 and 225x600 referred to as Grid-1, Grid-2, and Grid-3 respectively. Figure 4.2 shows the volume fraction distribution inside the annulus and the parameter used to check the grid independency. The parameter is the fully developed axial velocity. Percentage difference between all grids falls below 1%. Consequently, it was concluded that Grid-1 (100x266) is satisfactory and gives an accurate solution.

4.4 Validation

To check the adequacy of the present numerical solution, we compared the fully developed axial velocity profile of the numerical solution with the cor-
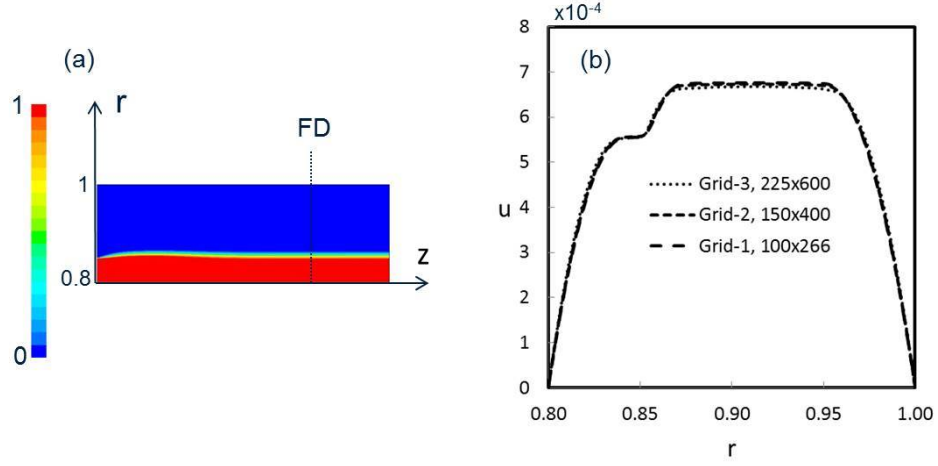
Figure 4.2: Full annulus model grid independence for Re_z=437.17, Re_θ=8.7, At=0, $B^{(1)}$=0.058 and $B^{(2)}$=0.035 : (a) volume fraction distribution: the red and blue colors denote the inner and outer fluids, respectively. (b) grid independence.

responding analytical solution as seen in figure 4.3. Here, the annulus has a radius ratio of 0.8. The inner fluid enters the annulus in the lower quarter of its gap.

Two cases (case1 and case2) were conducted to validate the numerical code. For case 1, figure 4.3-c, the average percentage difference between the numerical solution and the analytical solution lies within 2.8% difference indicating good agreement.

For the other case or case 2, we increase the two streams flow rates to test the code at different interface location. The comparison between the
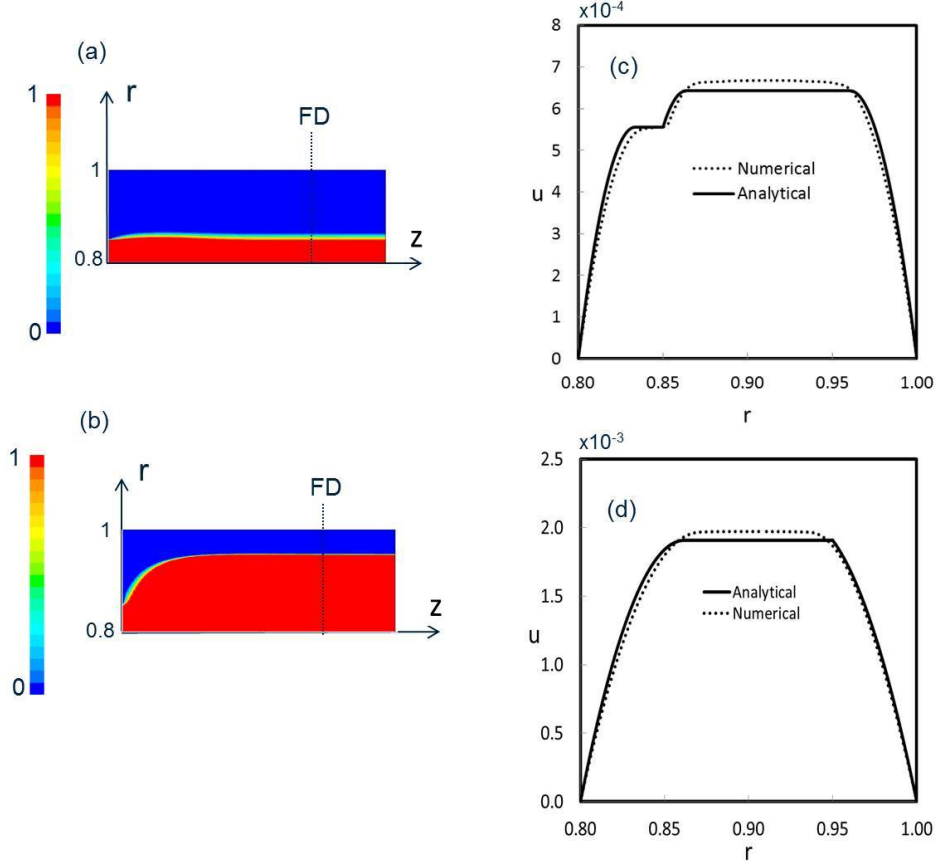
Figure 4.3:   Full annulus model validation with analytical solution: (a) volume fraction distribution for case 1, (b) volume fraction distribution for case 2, (c) validation (case 1: Re_z=437.17, Re_θ=8.7, At=0, $B^{(1)}$=0.058 and $B^{(2)}$=0.035) and (d) validation (case 2: for Re_z=820.57, Re_θ=8.7, At=0, $B^{(1)}$=0.031 and $B^{(2)}$=0.019). The red and blue colors denote the inner and outer fluids, respectively.

fully developed axial velocity profile of the numerical solution with the corresponding analytical solution for this case is shown in figure 4.3-d. The average percentage difference between the numerical solution and the analytical solution lies within 3% difference that reflects again a good agreement between the solutions.

4.5   Results

In this subsection we estimate the entrance length for the flow under consideration, track the interface location, look at the axial velocity profile development, explore the Kelvin Helmholtz instability related to the flow and present the results resulting from including the difference of density between layers.

4.5.1   Entrance length

Entrance length (L_e) for internal flow is the distance from inlet where the flow no longer changes with axial direction and is said to be fully developed. Downstream of entrance length, the velocity profile and wall shear are both constant, and the pressure drops linearly with axial direction, White (2003).

We set a criterion to calculate the entrance length as: the location at which the axial flow velocity reaches 98% of its fully developed value, figure

4.4-c. The volume fraction distribution and axial velocity contours for the same case are presented in parts a and b of figure 4.4, respectively.

We predict the entrance length of the Newtonian case for the creeping and laminar flow regimes with Reynolds number in the range of $Re_h \in (0.1 - 200)$ and predict the entrance length of the viscoplastic case for the creeping and laminar flow regimes with the value of Reynolds number in the range of $Re_h \in (0.1 - 10)$.

Our study results are represented together with previous results of the literature (Poole and Chhabra (2010) for pipe flow, McComas (1967) and Maia and Gasparetto (2003) for annular flow) in figure 4.4-d. A considerable amount of information can be gained from this figure. Firstly, the annular entrance length values are always considerably below the pipe values for the same Reynolds number. There are noticeable differences between the values reported in the literature for the same cases (same radius ratio and Reynolds number) for the entrance length in the laminar regime. The Newtonian fluid entrance length (L_e/D_h) approaches to a unique value as the Reynolds number goes to zero, the value is 0.28 in the case of radius ratio of 0.8. Visco-plastic fluids were found to have shorter entrance length for the same Reynolds number compared to Newtonian fluids in annuli.
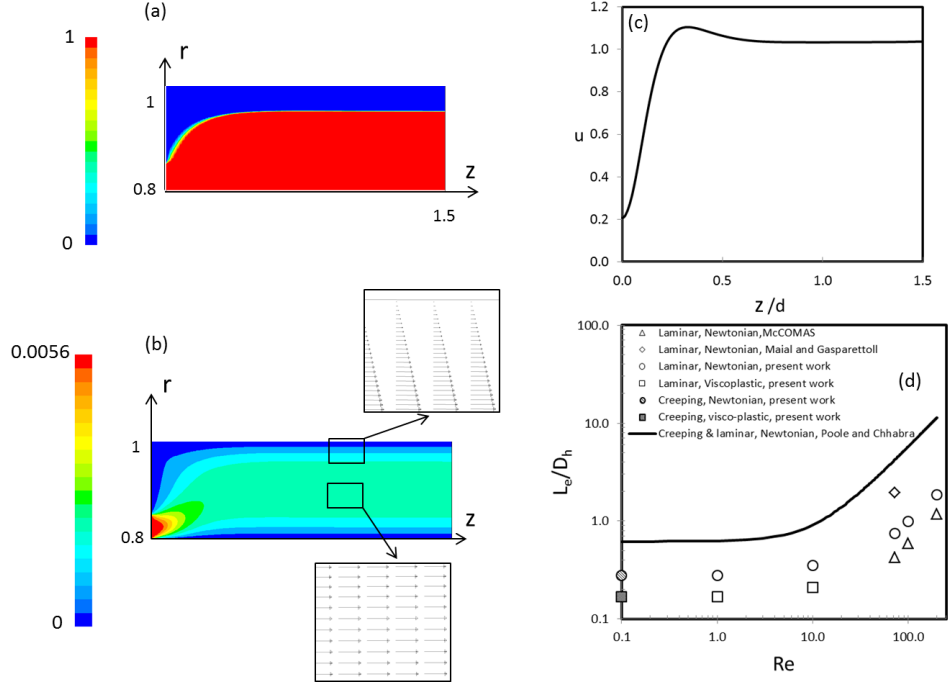
Figure 4.4: Entrance length. a) Volume fraction distribution: the red and blue colors denote the inner and outer fluids, respectively. b) axial velocity contours with enlarged views of velocity vectors near the wall and in mid-gap, c) Centerline velocity normalized with analytical fully developed value versus axial location, d) Entrance length for Newtonian and viscoplastic fluids in an annulus of radius ratio of 0.8.

4.5.2 Tracking the interface location

Tracking the interface location is an important task especially when it comes to fractionation efficiency. Figure 4.4-a shows the fluids volume fraction distribution in the flow, the sharp interface can be easily distinguished in the fully developed region compared to entry region. This may be attributed to the presence of transverse pressure in the inlet region. The fully developed location of the interface was at a radial location of 0.95. We have an excellent agreement between the numerical and the analytical values with the percentage difference falls below 1%.

4.5.3 Axial velocity profile development

Figure 4.5 shows the development of axial velocity profiles. The profiles at the inlets are flats (uniform velocity) for both the inner and outer fluids. It is clear that the flow is mostly yielded in the entrance region (z=0.05). This fact may be attributed to two factors. Firstly, while boundary layer approximation assumes constant lateral pressure (along each cross-section) in the fully developed region of the flow, the actual flow has a strong transverse pressure especially at inlets.

Only full elliptic equations can predict accurately the flow field characteristics in the entrance region (differences between parabolic and elliptic

differential equations are detailed in Appendix C). This behaviour was reported by Vradis et al. (1993) who reported a yielded axial velocity profile in the entrance region of a viscoplastic flow with a uniform inlet velocity profile. The numerical code used in this study (Ansys Fluent) has the capability to solve the full elliptic equations.

The second reason in our opinion for the flow to be yielded is something related to multi-layer viscoplastic flow nature, here, the inner and outer fluids compete in the entrance region exerting an additional pressure on each other through the interface. Initially, the inner fluid fills only 1/5 of the annular volume and is restricted by the inner wall. The only way to satisfy the non-slip condition at the inner wall is to expand toward the outer wall exerting more pressure on the outer fluid through the interface and leaving less space for the outer fluid to occupy. Consequently, this condition leads to more yielding in the outer fluid velocity profile.

4.5.4 Kelvin Helmholtz instability

When we consider parallel multi-layer flow with different layers velocities, it is important to check the Kelvin Helmholtz instability. The Kelvin Helmholtz instability occurs when there is a difference in velocity across the interface between two fluids of different densities. To check this instability, we set the
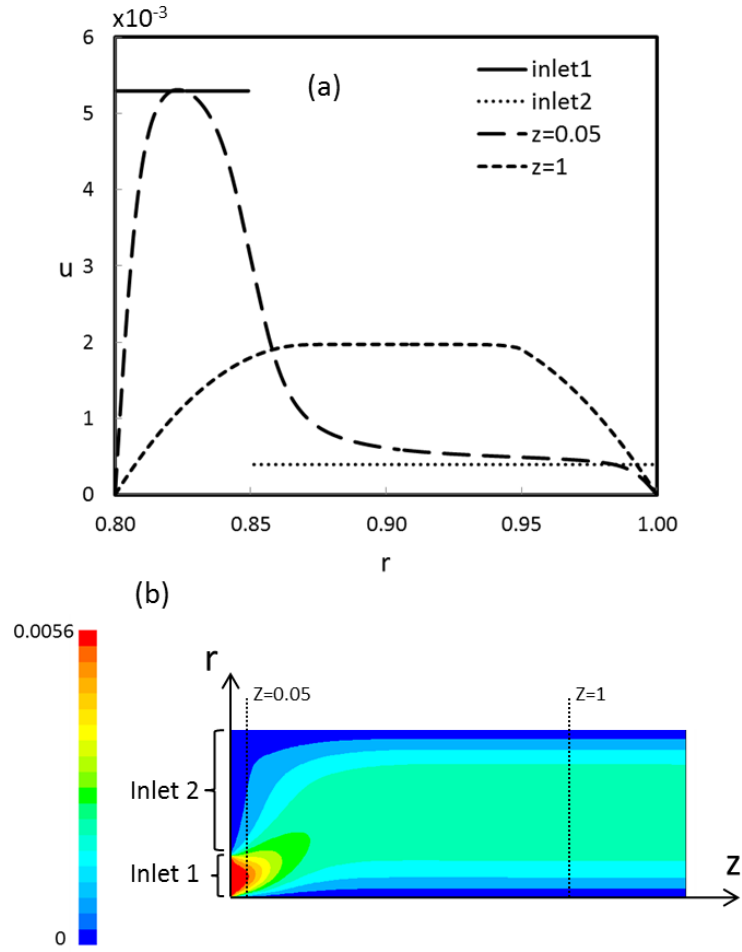
Figure 4.5:   Axial velocity profile development: a) Axial velocity profiles at inlets, entrance region and fully developed region. b) Axial velocity contours, Re_z=437.17, Re_θ=8.7, At=0, $B^{(1)}$=0.058 and $B^{(2)}$=0.035.

Richardson number to 0.08 which is way below the critical number according to Richardson Number Criterion.

The criterion states that the inequality $Ri < 1/4$ is a necessary condition for linear instability of inviscid stratified parallel flows. However, the criterion does not state that the flow is necessarily unstable if $Ri < 1/4$ somewhere, or even everywhere, in the flow.

Another requirement for this instability are Rayleighs inflection point and Fjortofts stronger condition criteria. They states that a necessary (but not sufficient) criterion for instability of an inviscid parallel flow is that the basic velocity profile has a point of inflection and the flow should satisfy the condition of $(u_{rr}(u - u_i) < 0)$ for all values of r, where u_{rr} is the second derivative of velocity and u_i is the velocity at the inflection points.

Please refer to figure 4.6 that shows the velocity profile at the inlet and immediately after the contact of the two fluids. Here due to the non-slip condition at the walls, mass continuity and the continuous nature of the velocity profile at the interface, the multi-layer velocity profile behaves as follow:

The slower stream (inner fluid) velocity profile adjusts instantaneously so that the minimum is zero at the wall and the maximum is at the interface. The faster stream (outer fluid) starts from zero value at the wall

and increases to a maximum value (above the inlet velocity) somewhere be-

tween the wall and the interface and then decreases to a lower value at the

interface. So essentially a zero velocity slope happens only once in the flow.

Although the velocity profile has two inflection points at around r=

0.85 and again around r = 0.9, the flow does not satisfy Fjortofts stronger

critierion since $(u_{rr}(u - u_i) > 0)$. It is worth mentioning that the Kelvin

Helmholtz instability is based on the inviscid flow where bounding walls are

not in the picture. We can conclude that the presence of walls stabilizes the

flow.
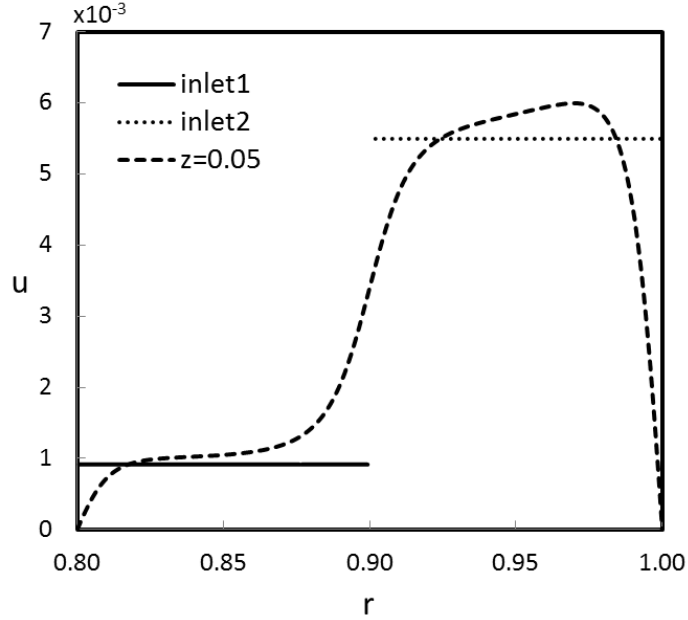
Figure 4.6: Axial velocity profiles, Re_z=5248, Re_θ=7.25, At=0.05, $B^{(1)}$=$B^{(2)}$=0 and Ri=0.08.

In the following section we include the density difference effect on the flow as this is the general case for the real (industrial) fluids densities.

4.5.5 Density difference effects

The previous results for both analytical and numerical solutions were produced based on the assumption of an iso-dense flow (which is most common) but there are some cases where the flow contains fluids of different densities. To address this, we set the Atwood number (At) to 0.2 to have the inner fluid as the heavier one (density unstable) or having the outer fluid as the heavier fluid (density stable). This value of Atwood number covers all ranges of Atwood number for the practical (industrial) combination of liquids.

We study the effect of rotational Reynolds number Re_θ and Bingham number, B to see the effect of the yield stress on rotating flow stability. In single fluid viscoplastic poisuielle flow in pipes and annuli, raising the yield stress has a stabilizing effect on the flow by elevating the critical Reynolds number, Re_c where the laminar flow starts to change to the turbulent regime, Hanks and Dadia (1971).

Figure 4.7 shows that Bingham number has a stabilizing effect on rotating flow. Here we do not have any mixing in the Newtonian case ($B^{(1)} = B^{(2)} = 0$) for the flow without rotation ($Re_\theta = 0$) as shown in figure 4.7-a.

When introducing the rotation ($Re_\theta = 166$) as shown in figure 4.7-b, and due to the unstable density situation (heavier inner fluid), the Newtonian case started to have some mixing. However, increasing Bingham numbers to ($B^{(1)} = B^{(2)} = 0062$) seems to prevent the mixing and the flow tends to be more stable, figure 4.7-c. Increasing further the Bingham numbers to ($B^{(1)} = B^{(2)} = 0064$) as shown in figure 4.7-d leads to a fully stable flow without any mixing.

For the density stable cases (with light inner fluid and heavy outer fluid) or for iso-dense cases (both fluids have the same density), the simulations showed that the flows are always stable.

In this chapter, we solve the spiral multi-layer viscoplastic flow inside a full annulus including the entrance region. We report the hydrodynamic entrance length for the flow in the lower range of laminar regime and the creeping regime for both Newtonian and viscoplastic fluids. We found that the entrance length of the viscoplastic flow is always smaller than the corresponding Newtonian flow for the same range of Reynolds number.

The Kelvin Helmholtz instability was not evident due to the presence of the walls of this bounded flow. The flow was always found to be stable for density stable or iso-dense cases. On the other hand, density unstable cases destabilize the flow but the flow can be stabilized by increasing the
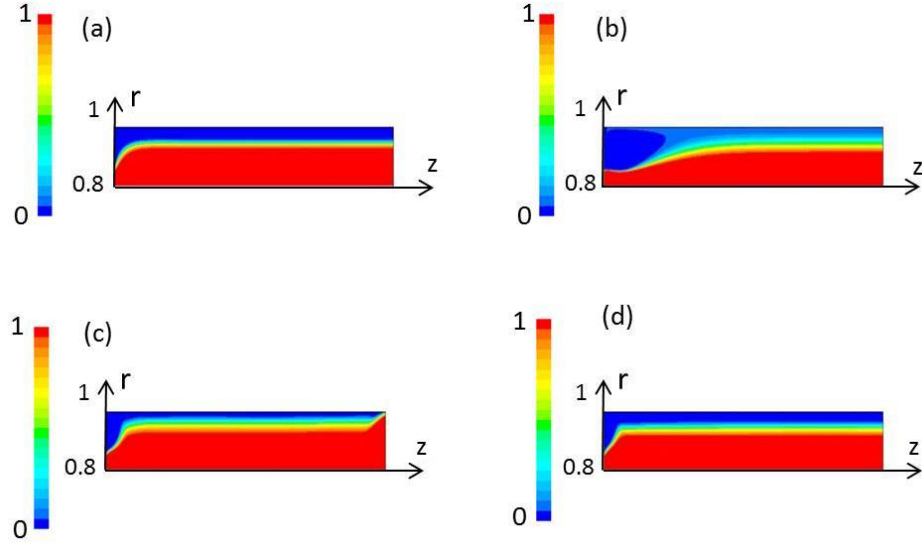
Figure 4.7: Density difference effect: Volume fraction distribution for At $= 0.2$ at: a) $Re_z = 403.26$, $Re_\theta = 0$ and $B^{(1)} = B^{(2)} = 0$, b) $Re_z = 424.60$, $Re_\theta = 166$ and $B^{(1)} = B^{(2)} = 0$, c) $Re_z = 20467.47$, $Re_\theta = 166$ and $B^{(1)} = B^{(2)} = 0.062$, d) $Re_z = 30006.11$, $Re_\theta = 166$ and $B^{(1)} = B^{(2)} = 0.064$. The red and blue colors denote the heavy and light fluids, respectively.

Bingham number (or increasing the yield stress).

Chapter 5

The continuous fractionation device and fractionation efficiency

Now with all information we conclude from the studies in the previous chapters, i.e., the fully developed flow solution study, the full annulus solution including the entrance region and the continuous fractionation study, we are able to design the full continuous fractionation device. We solve the flow inside the device and see the implications of the physical constraints of the device parts on the device operating parameters.

Our aim is to obtain a numerical solution for the full system of Navier stokes equations of the pressure driven laminar multi-layer viscoplastic fluid flow problem inside the continuous fractionation device. The walls of the device are rotating walls at a constant angular velocity.

5.1 Mathematical modeling and method of solution

We consider the fluid flow inside the continuous fractionation device geometry, figure 5.1. The dimensions were chosen based on the constraints resulted from the consideration of the intended range of operation (fluids flow rates and yield stresses values) and the available commercial pipe sizes.
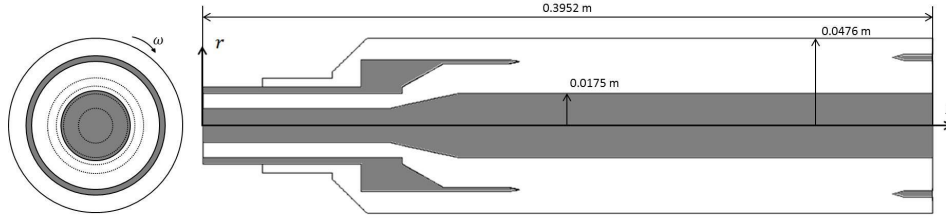
Figure 5.1: A schematic of the continuous fractionation device model geometry.

We follow the same approach that we use for the full annulus study (chapter 4) with the same assumptions and dimensionless groups. We follow also the same method of solution to solve numerically the flow under consideration. Same boundary conditions are defined with the exception of the outlet and walls boundary conditions that are defined as follow:

- At the outlet (z = 0.3952m):

We impose zero axial gradients at the (outflow condition in fluent).

- At the walls:

We impose the non-slip condition

$$u_z = 0$$

$$u_\theta = \hat{\omega}\hat{r}$$

We conduct several experiments to study the behaviour of the flow at different zones of the device. Our main parameter is the fluid flowrate ratios (Q_1/Q_2) that control the layers interface location, r_i. The interface location is a crucial factor that determines the efficiency of the fractionation as we show shortly in the discussion of the results section. Details of the runs conditions are shown in table 5.1.

5.2   Grid independence test

To achieve grid independence, the solution was computed for different grid sizes to assess the effects of mesh refinement. The grid sizes used were 55,000 cells, 105,000 cells and 155,000 cells referred to as Grid-1, Grid-2, and Grid-3 respectively. Figures 5.2 shows the parameter used to check the grid independency. The parameter is the fully developed axial velocity. Percentage difference between all grids falls below 1%. Consequently, it is

Q_1/Q_2	r_i
2.98	0.84
1.22	0.75
0.96	0.72
0.75	0.69
0.60	0.66

Table 5.1: A summary of the simulation runs conditions at: $Re_z = 149.3$, $Re_\theta = 7.88$, $B^{(1)} = 0.155$ and $B^{(2)} = 0.093$.

concluded that Grid-1 (105,000 cells) is satisfactory and gives an accurate solution.

5.3 Validation

To check the adequacy of the present computer code, we compared the fully developed axial velocity profile of the numerical solution with the corresponding analytical solution as seen in figure 5.3. The average percentage difference between the numerical solution and the analytical solution lies within 2 percent difference reflecting a good agreement.
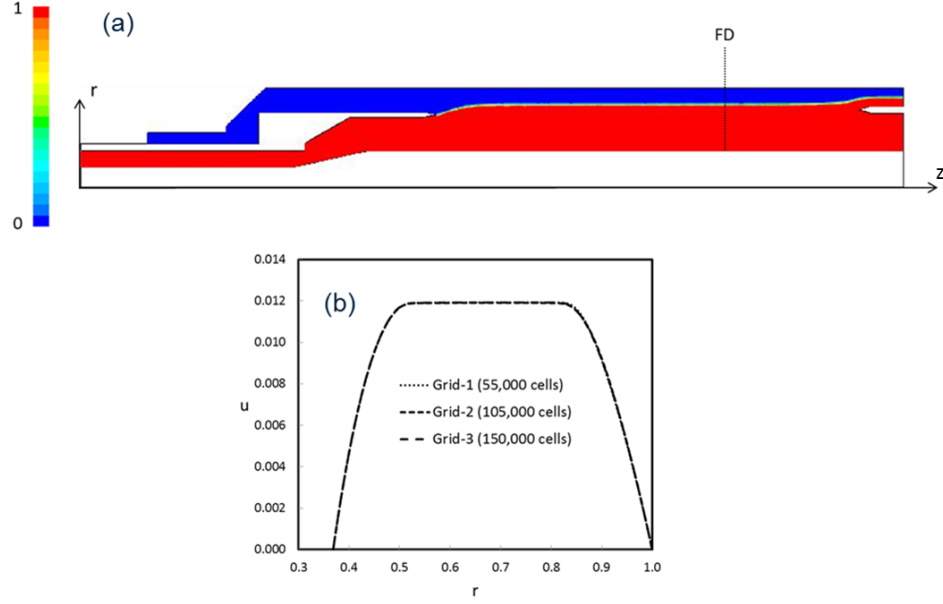
Figure 5.2: Fractionation device model grid independence for $Re_z = 149.3$, $Re_\theta = 7.88$, $B^{(1)} = 0.155$ and $B^{(2)} = 0.093$: (a) volume fraction distribution and (b) grid independence.

5.4   Results

In this section we track the development of the axial velocity profiles in different regions of the fractionation device and estimate the entrance length of the mixing region, we investigate the behaviour of the flow mainly the interface in the exit region of the device and predict the implications of this behaviour on the streams flowrates design and the size of the fractionation operating window.
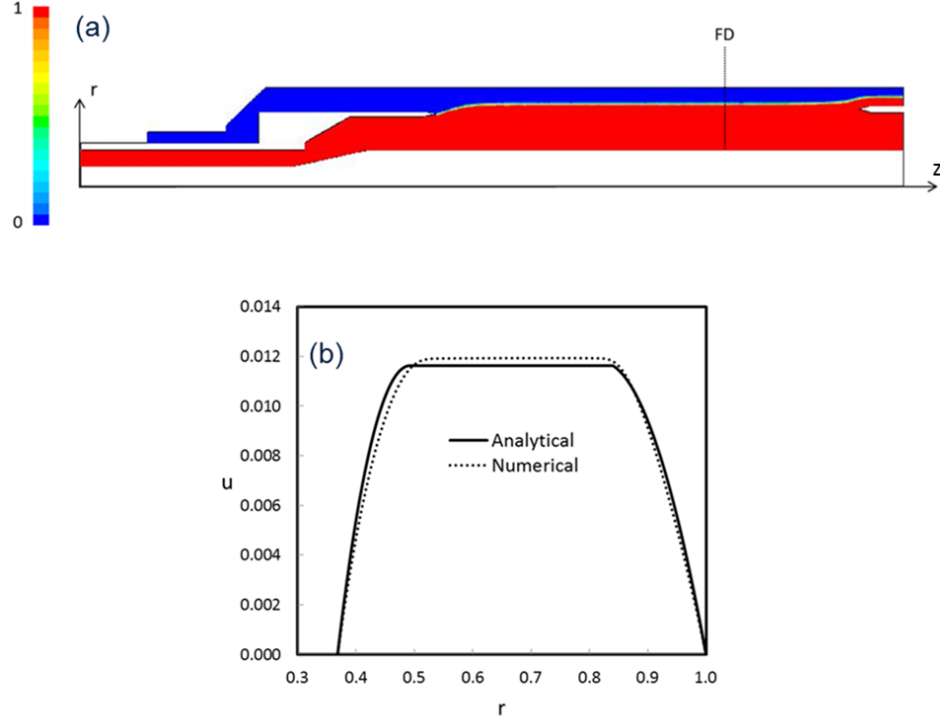
Figure 5.3: Fractionation device model validation with analytical solution at $Re_z = 149.3$, $Re_\theta = 7.88$, $B^{(1)} = 0.155$ and $B^{(2)} = 0.093$. (a) volume fraction distribution. (b) validation.

5.4.1 Axial velocity profile development and entrance length

Tracking the axial velocity profiles development is important to make sure that the flow reaches the fully developed condition early in the mixing zone in order to allow sufficient space for fractionation to take place. The mixing zone is the space where the two fluids meet between the inlet separator and

the outlet separator. Figure 5.4 shows the development of axial velocity profiles at different locations before, inside and after the mixing zone. Although the velocity profiles at the inlets are flat (uniform velocity), they develop downstream and adapt to fulfill the non-slip condition at walls (zero axial velocity at walls).

The velocity profiles reach the fully developed condition before and inside the mixing zone in this case, however, in the exit region (after mixing zone) and specifically the inner fluid stream outlet, the velocity profile do not reach the fully developed condition because the axial distance was not sufficient to cover the entrance length for that outlet.

The entrance length (L_e/D_h) was estimated to be in the order of 0.32. The value for the corresponding entrance length for a single viscoplastic fluid with the same value of Reynolds number was found to be 0.20 as reported in the previous chapter. This discrepancy is likely to be attributed to the fact that the current simulation is for the flow of two viscoplastic fluids flow.

In either case the entrance length is way below the corresponding entrance length of a viscoplastic pipe flow for the same range of Reynolds number. It is preferable to have a short entrance length as what we have in this case. This is because the time scale for the particles residence time in the entry region is small and the fractionation occurs solely in the fully

developed region of the mixing zone.
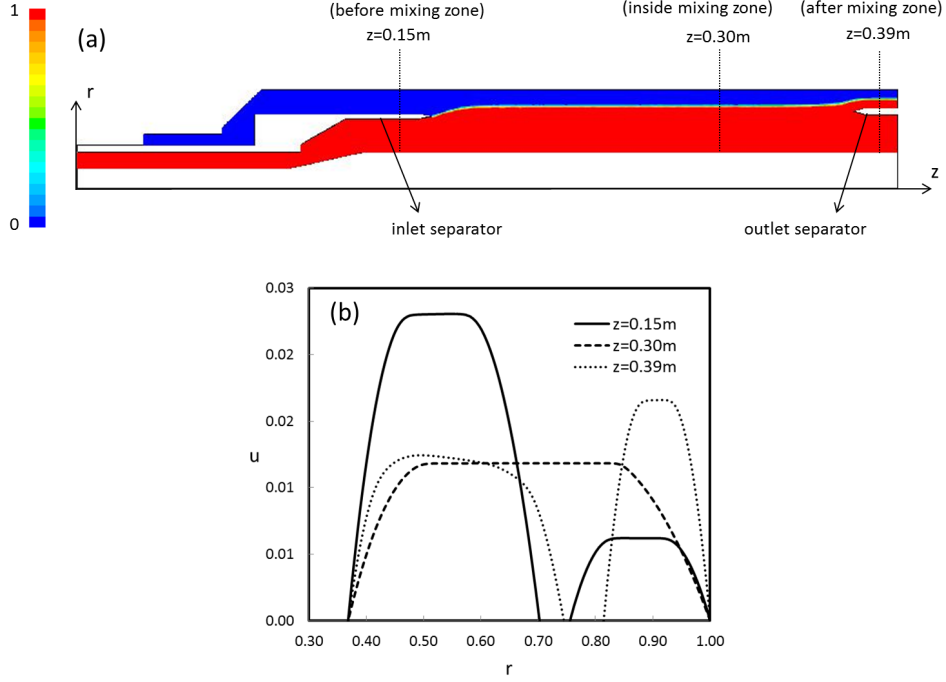
Figure 5.4: Axial velocity profile development: (a) Volume fraction distribution, (b) axial velocity profile development (before, inside and after mixing zone). Simulated at $Re_z = 149.3$, $Re_\theta = 7.88$, $B^{(1)} = 0.155$ and $B^{(2)} = 0.093$.

5.4.2 Outlet separator effects on interface

The presence of the outlet separator has an important effect on the flow characteristics especially the interface location as shown in figure 5.5. In the current simulation, the fluid interface in the fully developed region of

the mixing zone is located at a radial distance slightly higher than the radial distance of the outlet separator centerline. This situation makes the interface move out towards the outer wall since the flow has to satisfy the no-slip condition at the separator wall. Here, the interface tends to favor the areas of low shear stress in somewhere around the middle of the outer fluid outlet gap compared to the areas of high shear stress near the separator walls.
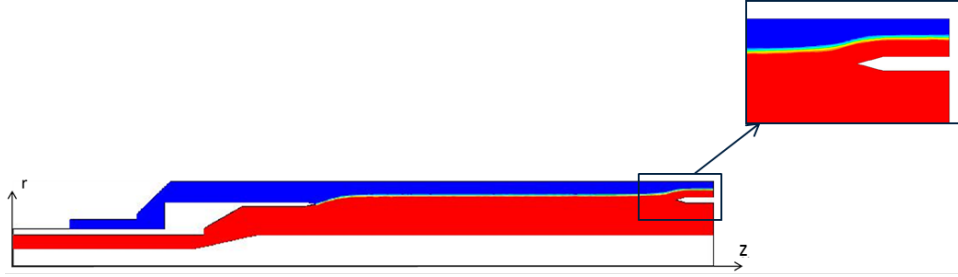
Figure 5.5: Fractionation device volume fraction distribution showing the effect of outlet separator on interface location, $Re_z = 149.3$, $Re_\theta = 7.88$, $B^{(1)} = 0.155$ and $B^{(2)} = 0.093$.

This phenomenon may lead to poor fractionation as some of the non-targeted particles may leave with the targeted (fractionated) particles through the outer fluid outlet. The flow needs to be designed (choosing the two streams flowrates) in a way that ensures that the interface of the fully developed region of the mixing zone is located radially below the outlet separator. This selection of flowrates leads to a successful fractionation by making sure that only targeted particles penetrate to the outer stream before they reach

87

axially the outlet separator.

5.4.3 Flow rates design

Additional simulations were carried out to investigate the behaviour of the flow at the exit region. Figure 5.6 shows the position of the interface for four different cases (simulations) as a result of the presence of the outlet separator. The separator physical location is bounded between the radial locations of (0.74 - 0.81). In the first two simulations when the values of the mixing zone fully developed interface were 0.84 and 0.75, the interface diverged to the outer fluid outlet (a situation that potentially hinders the fractionation efficiency).
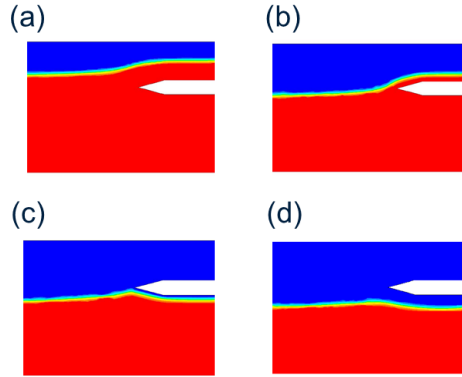
Figure 5.6: Interface behaviour at the exit region, $Re_z = 149.3$, $Re_\theta = 7.88$, $B^{(1)} = 0.155$ and $B^{(2)} = 0.093$ at: (a) $r_i = 0.84$, $Q_1/Q_2 = 2.98$, (b) $r_i = 0.75$, $Q_1/Q_2 = 1.22$, (c) $r_i = 0.72$, $Q_1/Q_2 = 0.96$ and (d) $r_i = 0.69$, $Q_1/Q_2 = 0.75$.

When we designed the flowrates to have the fully developed interface be located at 0.72, we noticed that the interface diverged to the inner fluid outlet (a favorable location in terms of fractionation efficiency) in close proximity to the separator. An interface of 0.69 would continue and exit freely the device through the inner fluid outlet.

We conclude that for this type of fractionation requirement and fluids rheology, the fluids flowrates need to be designed to have the maximum bound of the mixing zone interface to be 0.72 which corresponds to a flowrates ratio (Q_1/Q_2) of 0.96.

5.4.4   Exit region effects on fractionation diagram

To assess the device fractionation effectiveness especially with the disturbance in the exit region caused by the outlet separator, we demonstrate a specific fractionation case. We use the fractionation code that was developed and presented in chapter three to generate the required fractionation diagram.

In order to construct a fractionation diagram, we need to solve the flow in thousands of cases (a flow case has a unique combination of streams flowrates) in fluids of known properties. The analytical solution of chapter three is a feasible way to accomplish this task.

On the other hand, the numerical solutions as presented in chapters four and five would require several days to solve only one flow case. I generate a fractionation diagram for the case of fractionating a 2.5 mm sphere in a viscoplastic fluid suspension. The properties of the fractionation case are detailed in table 5.2. As shown in the fractionation diagram, figure 5.8, the operating window occupies a noticeable area of the diagram giving the operator flexibility with a wide range of flowrates to operate the device.

The time ratio in figure 5.8 is defined as the ratio between the residence and the settling times. The settling rate is the rate at which the particle travels radially across the gap, figure 5.7. This rate and the gap size represent the settling time in the chamber. The residence time on the other hand is the time spent as the particle travels axially through the mixing zone of the device. For fractionation to take place, the time ration has to be greater than unity.

When we include the effect of the outlet separator presence in the exit region, figure 5.9, the operating window is affected drastically and its coverage area shrunk considerably limiting the range of operation of the device. A relief of the operating window criterion from 50% (which is conservative in our opinion) to 40 or 30% would result in expanding the operating window.

Property	Value	Unit
Particles diameter	2.5	mm
Particles density	7800	kg/m^3
Suspension density	1000	kg/m^3
Annulus radius ratio	0.368	dimensionless
Annulus outer radius	0.0476	m
Inner and outer fluids plastic viscosity	1.083	$Pa.s$
Inner fluid yield stress	10	Pa
Outer fluid yield stress	6	Pa
Pressure drop/unit length range	750 to 5000	Pa/m
Rotation speed	40.22	rad/s

Table 5.2: fractionation case properties.
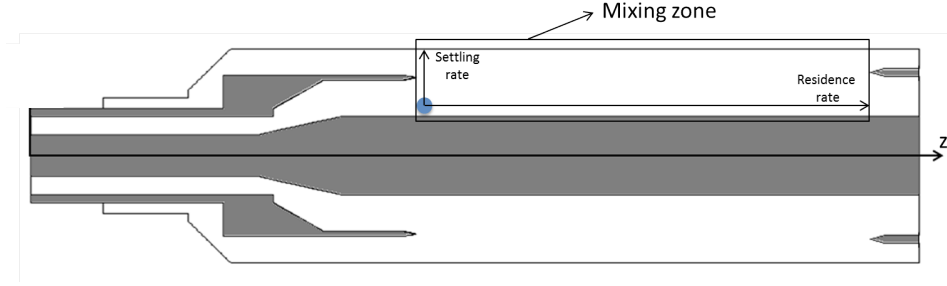
Figure 5.7: Settling and residence rates in the mixing zone of the device.

This measure could be used if the operator elects to increase the range of operation. The fractionation diagram will look like figures 5.10 and 5.11 if the operating window criterion is reduced to 40% and 30%, respectively.

In this chapter we design the continuous fractionation device based on the information we have from the fully developed, full annulus and continuous fractionation model studies. We validate the current code with the analytical solution. We track the velocity profile development to make sure that the flow reaches the fully developed condition early in the mixing zone to allow sufficient space for fractionation to take place. We study the exit region of the device and suggest certain guidelines to address the hurtful effect of the outlet separator on the layers interface and fractionation efficiency.
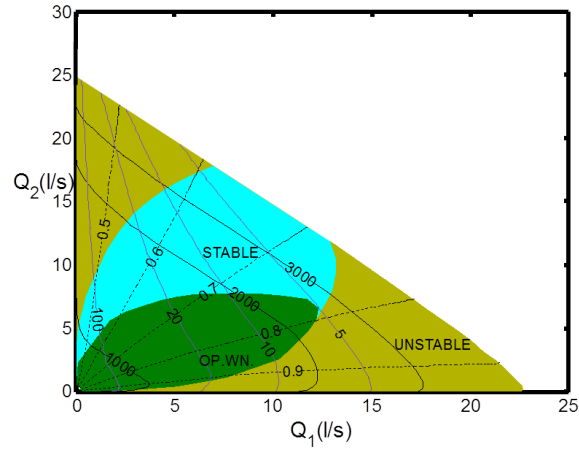
Figure 5.8: Fractionation diagram for the case detailed in table 5.2. Time ratios in blue lines, interface locations in black dashed lines and dimensionless pressure drop rate in solid black lines.
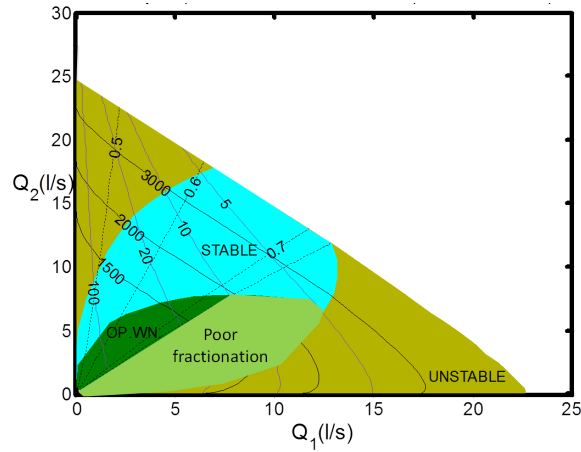
Figure 5.9: Fractionation diagram after including the effect of outlet separator. Case properties are per table 5.2. Time ratios in blue lines, interface locations in black dashed lines and dimensionless pressure drop rate in solid black lines.

Figure 5.10: Fractionation diagram for an operating window criterion of 40%. Case properties are per table 5.2. Time ratios in blue lines, interface locations in black dashed lines and dimensionless pressure drop rate in solid black lines.
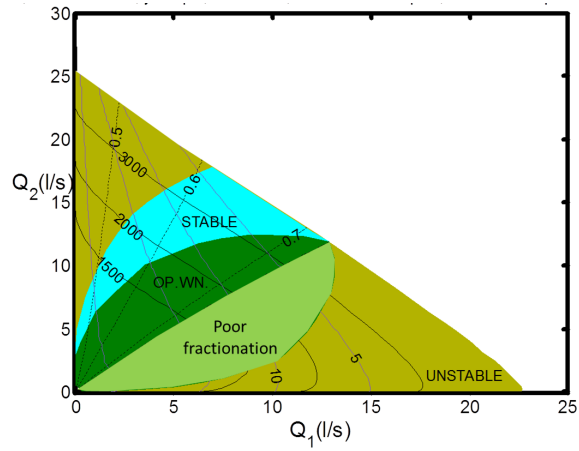
Figure 5.11: Fractionation diagram for an operating window criterion of 30%. Case properties are per table 5.2. Time ratios in blue lines, interface locations in black dashed lines and dimensionless pressure drop rate in solid black lines.
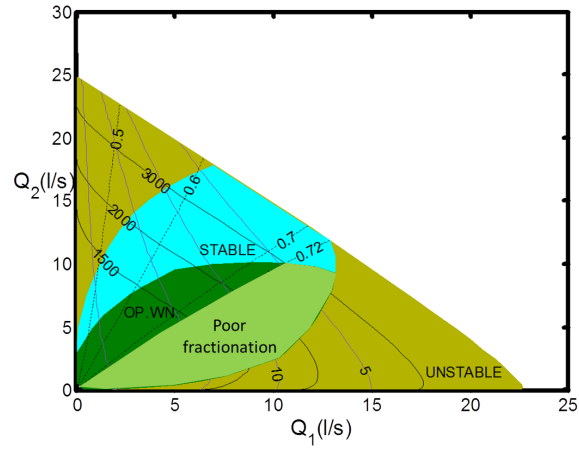
Chapter 6

Summary and conclusions

In this work we studied the application of the novel technology of particle suspension fractionation that was proposed by Madani et al. (2010b) on the continuous operation process. The flow that is suggested to be employed in facilitating this new fractionation methodology is the spiral multi-layer poisuille annular flow. Here we presented several studies of the flow in different circumstances/states namely: fully developed region, annular entry region and full fractionation device. We focused on the stability of the flow in conjunction with the fractionation requirement.

We found that spiral multi-layer Poisuille viscoplastic flow can be stable for both annulus and continuous fractionation geometries. The range of stability expands with increasing fluids yield stress as the yield stress supresses the yielded interfacial instability.

Gravity current instability was found to be evident in density unstable cases due to the centrifugal forces resulting from rotation and mixing can

happen in these cases. However, the flow can be stabilized by increasing the fluids yield stress (Bingham number). In the other hand, density current is not a factor in density stable and iso-dense cases.

Kelvin Helmholtz instability was not found on conditions tested. The presence of the walls in this internal flow has a stabilizing effect and prevents the onset of Kelvin Helmholtz instability.

All annular flows entrance lengths were found to be shorter than the corresponding ones of pipe flows for the same values of Reynolds number. We reported the hydrodynamic entrance length for the creeping and low range laminar flow regimes for annuli of both Newtonian and viscoplastic fluids. The entrance length of the viscoplastic flow was found to be shorter than the equivalent Newtonian flow for the same range of Reynolds number.

The disturbance to the flow at the exit region of the continuous fractionation device hinders the fractionation process due to the presence of the outlet separator. This situation adds more restriction to the fractionation operating window. In this regards, carful design of streams flowrates is crucial to providing a successful fractionation process.

Bibliography

MB Abbott. On the spreading of one fluid over another. *La Houille Blanche*, (6):827–856, 1961.

U Ts Andres. Equilibrium and motion of spheres in a viscoplastic liquid. In *Soviet Physics Doklady*, volume 5, page 723, 1961.

Byron E Anshus. Bingham plastic flow in annuli. *Industrial & Engineering Chemistry Fundamentals*, 13(2):162–164, 1974.

DIH Barr. Densimetric exchange flow in rectangular channels. *La Houille Blanche*, (6):619–632, 1967.

GK Batchelor. Sedimentation in a dilute dispersion of spheres. *Journal of fluid mechanics*, 52(02):245–268, 1972.

T Brooke Benjamin. Gravity currents and related phenomena. *Journal of Fluid Mechanics*, 31(02):209–248, 1968.

AN Beris, JA Tsamopoulos, RC Armstrong, and RA Brown. Creeping

motion of a sphere through a bingham plastic. *Journal of Fluid Mechanics*, 158:219–244, 1985.

SH Bittleston, J Ferguson, and IA Frigaard. Mud removal and cement placement during primary cementing of an oil well–laminar non-newtonian displacements in an eccentric annular hele-shaw cell. *Journal of Engineering Mathematics*, 43(2-4):229–253, 2002.

Simon H Bittleston and Ole Hassager. Flow of viscoplastic fluids in a rotating concentric annulus. *Journal of non-newtonian fluid mechanics*, 42(1):19–36, 1992.

Jason E Butler and Eric SG Shaqfeh. Dynamic simulations of the inhomogeneous sedimentation of rigid fibres. *Journal of Fluid Mechanics*, 468: 205–237, 2002.

SS Chen, LT Fan, and CL Hwang. Entrance region flow of the bingham fluid in a circular pipe. *AIChE Journal*, 16(2):293–299, 1970.

Raj P Chhabra. *Bubbles, drops, and particles in non-Newtonian fluids*. CRC press, 2006.

MR Chowdhury and Firat Yener Testik. Viscous propagation of two-

dimensional non-newtonian gravity currents. *Fluid Dynamics Research*, 44(4):045502, 2012.

V Ciriello, S Longo, L Chiapponi, and V Di Federico. Porous gravity currents of non-newtonian fluids within confining boundaries. *Procedia Environmental Sciences*, 25:58–65, 2015.

JJ Derksen et al. Direct simulations of spherical particle motion in bingham liquids. *Computers & Chemical Engineering*, 35(7):1200–1214, 2011.

V Di Federico, S Malavasi, and G Bizzarri. Viscous spreading of non-newtonian gravity currents in radial geometry. *WIT Trans Eng Sci*, 52: 399–408, 2006a.

V Di Federico, R Archetti, and S Longo. Spreading of axisymmetric non-newtonian power-law gravity currents in porous media. *Journal of Non-Newtonian Fluid Mechanics*, 189:31–39, 2012.

Vittorio Di Federico, Stefano Malavasi, and Stefano Cintoli. Viscous spreading of non-newtonian gravity currents on a plane. *Meccanica*, 41(2):207–217, 2006b.

F Durst, S Ray, B Ünsal, and OA Bayoumi. The development lengths of

laminar pipe and channel flows. *Journal of fluids engineering*, 127(6): 1154–1160, 2005.

MP Escudier, PJ Oliveira, and FT Pinho. Fully developed laminar flow of purely viscous non-newtonian liquids through annuli, including the effects of eccentricity and inner-cylinder rotation. *International Journal of Heat and Fluid Flow*, 23(1):52–73, 2002.

EE Feldman, RW Hornbeck, et al. A numerical solution of laminar developing flow in eccentric annular ducts. *International journal of heat and mass transfer*, 25(2):231–241, 1982.

James Feng, Howard H Hu, and Daniel D Joseph. Direct simulation of initial value problems for the motion of solid bodies in a newtonian fluid part 1. sedimentation. *Journal of Fluid Mechanics*, 261:95–134, 1994.

Michael McNeil Forbes, A. Apple, and B. Boat. Frequency of quality testing in syrup creation. *Maple Science J.*, 255:139–144, 2010.

Edmund J Fordham, Simon H Bittleston, and M Ahmadi Tehrani. Viscoplastic flow in centered annuli, pipes, and slots. *Industrial & Engineering Chemistry Research*, 30(3):517–524, 1991.

Arnold Fredrickson and R Byron Bird. Non-newtonian flow in annuli. *Industrial & Engineering Chemistry*, 50(3):347–352, 1958.

IA Frigaard. Super-stable parallel flows of multiple visco-plastic fluids. *Journal of non-newtonian fluid mechanics*, 100(1):49–75, 2001.

Julio Gratton, Fernando Minotti, and Swadesh M Mahajan. Theory of creeping gravity currents of a non-newtonian liquid. *Physical Review E*, 60(6):6960, 1999.

IP Grinchik and A Kh Kim. Axial flow of a nonlinear viscoplastic fluid through cylindrical pipes. *Journal of Engineering Physics and Thermophysics*, 23(2):1039–1041, 1972.

Richard W Hanks. The axial laminar flow of yield-pseudoplastic fluids in a concentric annulus. *Industrial & Engineering Chemistry Process Design and Development*, 18(3):488–493, 1979.

Richard W Hanks and Bharat H Dadia. Theoretical analysis of the turbulent flow of non-newtonian slurries in pipes. *AIChE Journal*, 17(3):554–557, 1971.

J Happel and H Brenner. Low reynolds number hydrodynamics. 1965, 1965.

Howard S Heaton, William C Reynolds, and William M Kays. Heat trans-

fer in annular passages. simultaneous development of velocity and temperature fields in laminar flow. *International Journal of Heat and Mass Transfer*, 7(7):763–781, 1964.

Benjamin Herzhaft and Élisabeth Guazzelli. Experimental study of the sedimentation of dilute and semi-dilute suspensions of fibres. *Journal of Fluid Mechanics*, 384:133–158, 1999.

Richard Holm, S Storey, Mark Martinez, and L Daniel Söderberg. Visualization of streaming-like structures during settling of dilute and semi-dilute rigid fibre suspensions. *Physics of fluids*, 2004.

CK Huen, IA Frigaard, and DM Martinez. Experimental studies of multi-layer flows using a visco-plastic lubricant. *Journal of non-newtonian fluid mechanics*, 142(1):150–161, 2007.

KOLF Jayaweera and BJ Mason. The behaviour of freely falling cylinders and cones in a viscous fluid. *Journal of Fluid Mechanics*, 22(04):709–720, 1965.

Lin Jianzhong, Shi Xing, and You Zhenjiang. Effects of the aspect ratio on the sedimentation of a fiber in newtonian fluids. *Journal of Aerosol Science*, 34(7):909–921, 2003.

Laurent Jossic and Albert Magnin. Drag and stability of objects in a yield stress fluid. *AIChE journal*, 47(12):2666–2672, 2001.

F Julien Saint Amand and B Perrin. Fundamentals of screening: Effect of rotor design and fibre properties. *Proceedings of the Tappi Pulping Confernce*, pages 941–955, 1999.

Donald L Koch and Eric SG Shaqfeh. The instability of a dispersion of sedimenting spheroids. *Journal of Fluid Mechanics*, 209:521–542, 1989.

P Kumar and BV Ramarao. Enhancement of the sedimentation rates of fibrous suspensions. *Chemical Engineering Communications*, 108(1):381–401, 1991.

Peter B Laxton and John C Berg. Gel trapping of dense colloids. *Journal of colloid and interface science*, 285(1):152–157, 2005.

Yu-Quan Liu and Ke-Qin Zhu. Axial couette–poiseuille flow of bingham fluids through concentric annuli. *Journal of Non-Newtonian Fluid Mechanics*, 165(21):1494–1504, 2010.

S Longo, V Di Federico, and L Chiapponi. Propagation of viscous gravity currents inside confining boundaries: the effects of fluid rheology and channel geometry. In *Proceedings of the Royal Society of London A: Math-*

ematical, Physical and Engineering Sciences, volume 471, page 20150070. The Royal Society, 2015.

Sandro Longo, Vittorio Di Federico, Renata Archetti, Luca Chiapponi, Valentina Ciriello, and Marius Ungarish. On the axisymmetric spreading of non-newtonian power-law gravity currents of time-dependent volume: an experimental and theoretical investigation focused on the inference of rheological parameters. *Journal of Non-Newtonian Fluid Mechanics*, 201: 69–79, 2013.

Michael B Mackaplow and Eric SG Shaqfeh. A numerical study of the sedimentation of fibre suspensions. *Journal of Fluid Mechanics*, 376:149–182, 1998.

A Madani, S Storey, JA Olson, IA Frigaard, J Salmela, and DM Martinez. Fractionation of non-brownian rod-like particle suspensions in a viscoplastic fluid. *Chemical Engineering Science*, 65(5):1762–1772, 2010a.

A. Madani, D.M. Martinez, J.A. Olson, and I.A. Frigaard. The stability of spiral poiseuille flows of newtonian and bingham fluids in an annular gap. *Journal of Non-Newtonian Fluid Mechanics*, 193:3 – 10, 2013.

Ario Madani, James A Olson, D Mark Martinez, and Alan Fung. Novel

methods to characterize and fractionate papermaking fibres. *Nordic Pulp & Paper Research Journal*, 25(4):448–455, 2010b.

Ario Madani, Harri Kiiskinen, James A Olson, and D Mark Martinez. Fractionation of microfibrillated cellulose and its effects on tensile index and elongation of paper. *NORDIC PULP & PAPER RESEARCH JOURNAL*, 26(3):306–311, 2011.

MCA Maia and CA Gasparetto. A numerical solution for the entrance region of non-newtonian flow in annuli. *Brazilian Journal of Chemical Engineering*, 20(2):201–211, 2003.

R Marton and JD Robie. Characterization of mechanical pulps by a settling technique. *Tappi Tech Ass Pulp Pap Indus*, 1969.

ST McComas. Hydrodynamic entrance lengths for ducts of arbitrary cross section. *Journal of Basic Engineering*, 89(4):847–850, 1967.

Olivier FJ Meuric, Richard J Wakeman, Tak W Chiu, and Kenneth A Fisher. Numerical flow simulation of viscoplastic fluids in annuli. *The Canadian Journal of Chemical Engineering*, 76(1):27–40, 1998.

Taegee Min, Hyoung Gwon Choi, Jung Yul Yoo, and Haecheon Choi. Laminar convective heat transfer of a bingham plastic in a circular pipeii. nu-

merical approach hydrodynamically developing flow and simultaneously developing flow. *International Journal of Heat and Mass Transfer*, 40(15): 3689–3701, 1997.

MA Moyers-Gonzalez, IA Frigaard, and C Nouar. Nonlinear stability of a visco-plastically lubricated viscous shear flow. *Journal of Fluid Mechanics*, 506:117–146, 2004.

C Nouar. Numerical and experimental investigation of thermal convection for thermodependent herschel-bulkley fluid in an annular duct with rotating inner cylinder. In *Progress and Trends in Rheology V*, pages 297–298. Springer, 1998.

Z Nowak and B. Gajdeczko. Laminar entrace region flow of the bingham fluid. *Acta Mechanica*, 49(3):191–200, 1983.

Shinichi Ookawara, Kohei Ogawa, Norman Dombrowski, Esmail Amooie-Foumeny, and Ahmed Riza. Unified entry length correlation for newtonian, power law and bingham fluids in laminar pipe flow at low reynolds number. *Journal of chemical engineering of Japan*, 33(4):675–678, 2000.

L Paavilainen. The possibility of fractionating softwood sulfate pulp according to cell wall thickness. *Appita*, 45(5):319–326, 1992.

Tasos C Papanastasiou. Flows of materials with yield. *Journal of Rheology (1978-present)*, 31(5):385–404, 1987.

JP Pascal. A two-layer model for a non-newtonian gravity current subjected to wind shear. *Acta mechanica*, 162(1-4):83–98, 2003.

Suhas Patankar. *Numerical heat transfer and fluid flow.* CRC press, 1980.

S Pelipenko and IA Frigaard. Mud removal and cement placement during primary cementing of an oil well–part 2; steady-state displacements. *Journal of Engineering Mathematics*, 48(1):1–26, 2004.

Jie Peng and Ke-Qin Zhu. Linear stability of bingham fluids in spiral couette flow. *Journal of Fluid Mechanics*, 512:21–45, 2004.

RJ Poole and RP Chhabra. Development length requirements for fully developed laminar pipe flow of yield stress fluids. *Journal of Fluids Engineering*, 132(3):034501, 2010.

RJ Poole and BS Ridley. Development-length requirements for fully developed laminar pipe flow of inelastic non-newtonian liquids. *Journal of Fluids Engineering*, 129(10):1281–1287, 2007.

AMV Putz, TI Burghelea, IA Frigaard, and DM Martinez. Settling of an

isolated spherical particle in a yield stress shear thinning fluid. *Physics of Fluids*, 20(3):33102–33300, 2008.

J Salmela, DM Martinez, and M Kataja. Settling of dilute and semidilute fiber suspensions at finite re. *AIChE journal*, 53(8):1916–1923, 2007.

RK Shah. A correlation for laminar hydrodynamic entry length solutions for circular and noncircular ducts. *Journal of Fluids Engineering*, 100(2): 177–179, 1978.

VL Shah and RJ Soto. Entrance flow of a bingham fluid in a tube. *Applied Scientific Research*, 30(4):271–278, 1975.

Lawrence F Shampine, Robert Ketzscher, and Shaun A Forth. Using ad to solve bvps in matlab. *ACM Transactions on Mathematical Software (TOMS)*, 31(1):79–94, 2005.

ZP Shul'Man. Calculation of a laminar axial flow of a nonlinear viscoplastic medium in an annular channel. *Journal of engineering physics*, 19(4): 1283–1289, 1970.

John E Simpson. Gravity currents in the laboratory, atmosphere, and ocean. *Annual Review of Fluid Mechanics*, 14(1):213–234, 1982.

John E Simpson. *Gravity currents: In the environment and the laboratory.* Cambridge university press, 1999.

C.M. Sloane. Kraft pulp processing - pressure screen fractionation . *Appita J.*, 53(3):220226, 2000.

Hervé Tabuteau, Philippe Coussot, and John R de Bruyn. Drag force on a sphere in steady motion through a yield-stress fluid. *Journal of Rheology (1978-present)*, 51(1):125–137, 2007.

D Vola, F Babik, and J-C Latché. On a numerical strategy to compute gravity currents of non-newtonian fluids. *Journal of computational physics*, 201(2):397–420, 2004.

George C Vradis, John Dougher, and Sunil Kumar. Entrance pipe flow and heat transfer for a bingham plastic. *International journal of heat and mass transfer*, 36(3):543–552, 1993.

Yeh Wang. Finite element analysis of the duct flow of bingham plastic fluids: an application of the variational inequality. *International journal for numerical methods in fluids*, 25(9):1025–1042, 1997.

YEH Wang. Axial flow of generalized viscoplastic fluids in non-circular ducts. *Chemical Engineering Communications*, 168(1):13–43, 1998.

Frank M White. Fluid mechanics. 5th. *Boston: McGraw-Hill Book Company*, 2003.

Appendix A

Fluid rheology and stability

The following figures A.1, A.2, A.3 and A.4 show the effect of the outer fluid yield stress, inner and outer fluids plastic viscosity and radius ratio on the flow stability.

In addition, we present figure A.5 in which we specify the maximum flow rate Q that may be reached while maintaining a successful separation or in other words, having the residence to settling time ratio of unity.
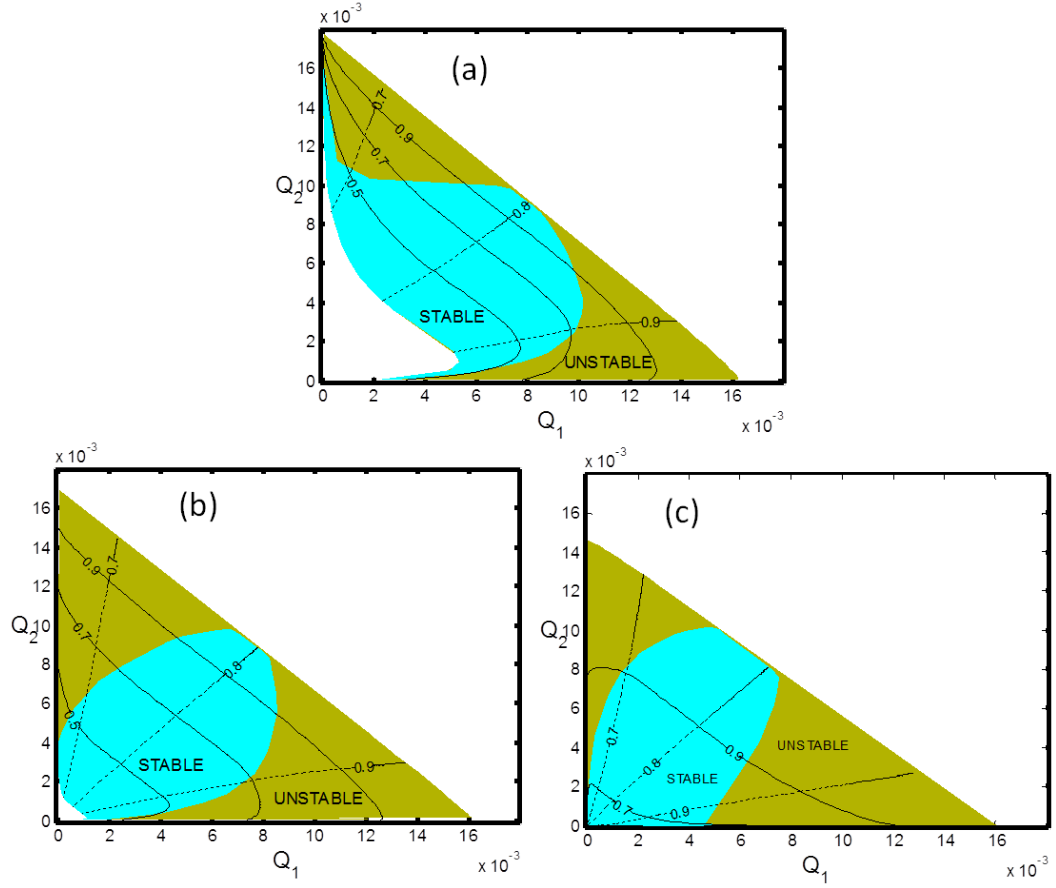
Figure A.1: The solution of equations 3.22-3.23 for the conditions given as series 2 in table 3.1. The colour map defines the stability of the flow state, as given in figure 3.3. The dashed line represents the interface position and the solid line represents the pressure drop rate: (a) $\tau_y^{(2)} = 0$, (b) $\tau_y^{(2)} = 0.5$, (c) $\tau_y^{(2)} = 2$.
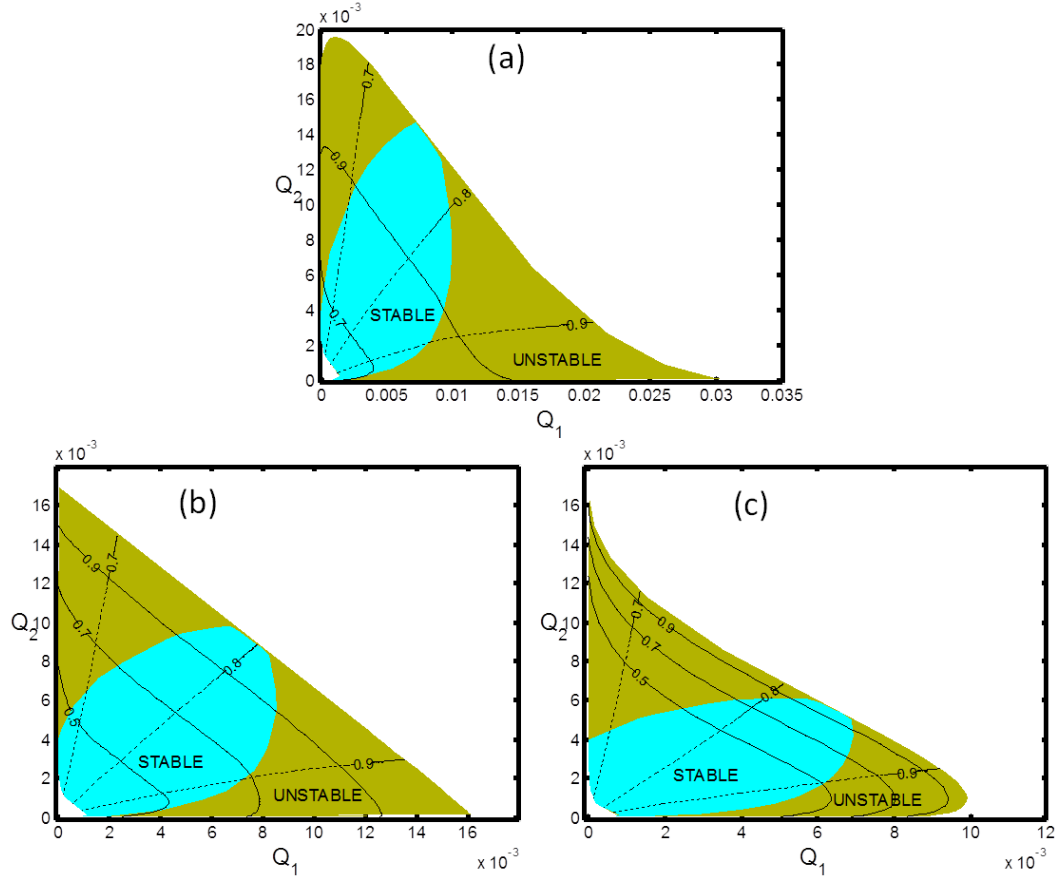
Figure A.2: The solution of equations 3.22-3.23 for the conditions given as series 3 in table 3.1. The colour map defines the stability of the flow state, as given in figure 3.3. The dashed line represents the interface position and the solid line represents the pressure drop rate: (a) $\mu^{(1)} = 0.375$, (b) $\mu^{(1)} = 0.75$, (c) $\mu^{(1)} = 1.5$.
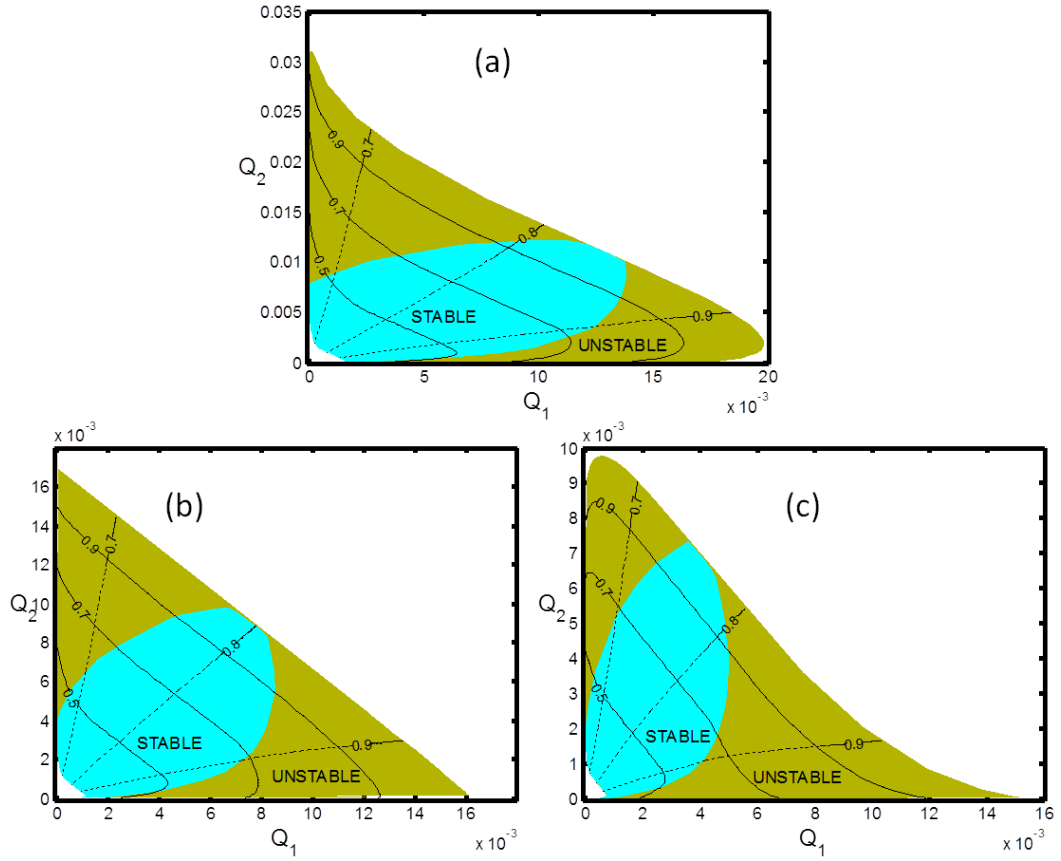
Figure A.3:   The solution of equations 3.22-3.23 for the conditions given as series 4 in table 3.1. The colour map defines the stability of the flow state, as given in figure 3.3. The dashed line represents the interface position and the solid line represents the pressure drop rate: (a) $\mu^{(2)} = 0.375$, (b) $\mu^{(2)} = 0.75$, (c) $\mu^{(2)} = 1.5$.
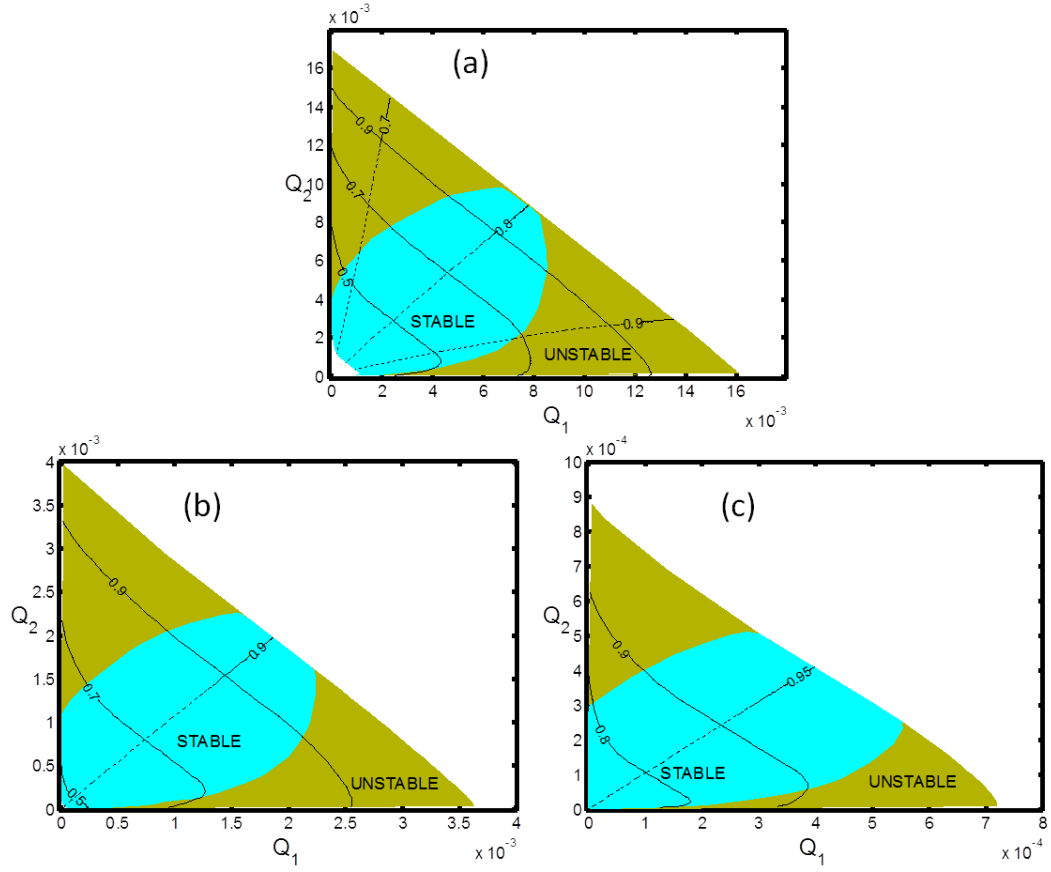
Figure A.4: The solution of equations 3.22-3.23 for the conditions given as series 5 in table 3.1. The colour map defines the stability of the flow state, as given in figure 3.3. The dashed line represents the interface position and the solid line represents the pressure drop rate: (a) $\kappa = 0.6$, (b) $\kappa = 0.8$, (c) $\kappa = 0.9$.
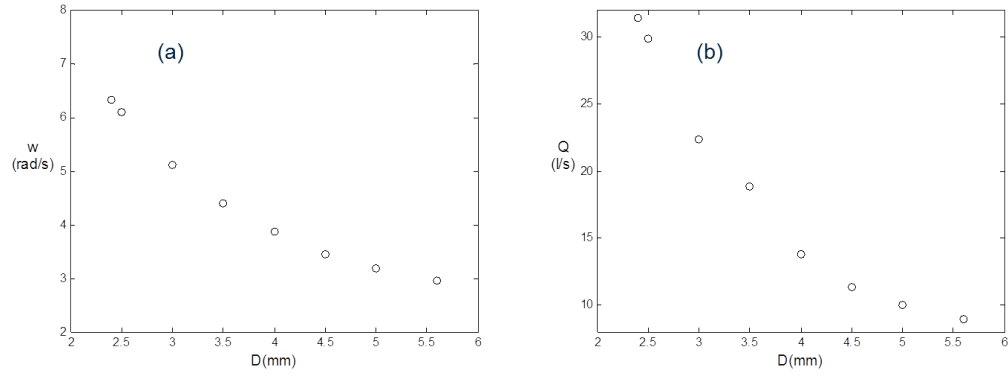
Figure A.5: Maximum allowable flow rates Q in (l/s) for different stainless steel spherical particles in a fluid having a yield stress $\tau_y = 1\ Pa$. The annulus axial length $L = 50\ cm$, radius ratio, $\kappa = 0.6$, outer radius, $R = 0.127\ m$, plastic viscosity, $\mu = 1.0833\ Pa.s$, spheres density, $\rho_s = 7800\ kg/m^3$ and suspension density, $\rho_f = 1000\ kg/m^3$: a) fractionation curve, b) maximum allowable flow rates.

Appendix B

Fractionation computer program operation

In order to find the operating curves for a specific case i.e. (specific fluids rheology and geometries and properties of targeted fractionated particles), we need to follow some steps to define these properties and parameters and feed them to the program we developed in this concern:

Inputs:

- Set the annulus geometry parameters, radius ratio, κ (dimensionless) and outer radius, $\hat{R}$ (m).

- Set the rotational speed, $\hat{\omega}$ (rad/s) required to fractionate specific particles that have their specific size, $\hat{D}$ (m) and density, $\hat{\rho}_s$.

- Set the fluids physical and rheological properties, inner fluid yield stress and plastic viscosity, $\hat{\tau}_{y1}$ (pa) , $\hat{\mu}^{(1)}$ (Pa.s), outer fluid yield

stress and plastic viscosity, $\hat{\tau}_{y2}$ (pa) , $\hat{\mu}^{(2)}$ (Pa.s) and fluids density $\hat{\rho}_f$.

- Set up ranges for independent variables, interface radius, r_i (dimensionless) and pressure drop, $\hat{G}$ (Pa/m).

- Run the program.

Outputs:

- Velocities profiles (axial and circumferential for both inner and outer fluids).

- Flow rates.

- Stability conditions.

- The operating window.

Appendix C

Parabolic equations versus elliptic partial differential equations

The following general second order partial differential equation can be classified as an elliptic or a parabolic partial differential equation based on the parameter $(b^2 - 4ac)$. The partial differential equation is classified as parabolic if $(b^2 - 4ac)$ is zero and classified as elliptic if $(b^2 - 4ac)$ is negative.

$$au_{xx} + bu_{xr} + cu_{rr} + du_x + eu_r + fu = g$$

Where $(u_{xx}, u_{xr}$ and $u_{rr})$ are second order partial derivatives and $(u_x$ and $u_r)$ are first order partial derivatives. $(a, b, c, d, e, f$ and $g)$ are constants or functions of independent variables $(x$ and $r)$.

The governing equations of the present study are elliptic partial differ-

ential equations because both second order partial derivatives (u_{rr} and u_{xx}) do exist. Elliptic partial differential equations govern the equilibrium problems in which the solution of the partial differential equations is desired in a closed domain subject to a prescribed set of boundary conditions. In this case, the solution of the partial differential equations at every point in the domain depends upon the prescribed boundary condition at every point on the boundaries.

Researchers mostly simplify the Navier stockes equations using the boundary layer approximation. They neglect the second order partial derivative (u_{xx}) and the only second order partial derivative left in the equations was (u_{rr}). This led to changing the elliptic nature of the partial differential equation to a parabolic nature.

Parabolic partial differential equations govern the marching or propagation problems where the solution of the partial differential equations is required on an open domain subject to a set of initial conditions and a set of boundary conditions. The solution must be computed by marching outward from the initial data surface while satisfying the boundary conditions.